

**DETECTING THE SPATIOTEMPORAL DYNAMICS OF NEURAL
ACTIVITY ON THE CORTICAL SURFACE: APPLYING
ANATOMICALLY CONSTRAINED BEAMFORMING TO EEG**

by

Vyacheslav Murzin

A Dissertation Submitted to the Faculty of
The Charles E. Schmidt College of Science
in Partial Fulfillment of the Requirements for the Degree of
Doctor of Philosophy

Florida Atlantic University

Boca Raton, FL

May 2010

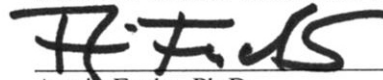
DETECTING THE SPATIOTEMPORAL DYNAMICS OF NEURAL
ACTIVITY ON THE CORTICAL SURFACE: APPLYING
ANATOMICALLY CONSTRAINED BEAMFORMING TO EEG.

by

Vyacheslav L. Murzin

This dissertation was prepared under the direction of the candidate's dissertation advisor, Dr. Armin Fuchs, Physics Department, and has been approved by the members of his supervisory committee. It was submitted to the faculty of the Charles E. Schmidt College of Science and was accepted in partial fulfillment of the requirements for the degree of Doctor of Philosophy.

SUPERVISORY COMMITTEE:

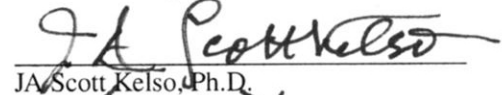


Armin Fuchs, Ph.D.


Dissertation Advisor



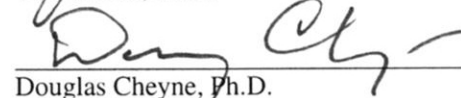
Warner Miller, Ph.D.



JA Scott Kelso, Ph.D.



Viktor Jirsa, Ph.D.

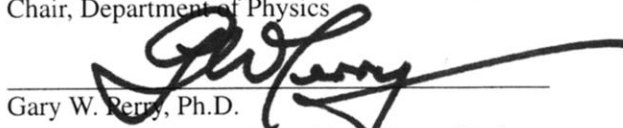


Douglas Cheyne, Ph.D.



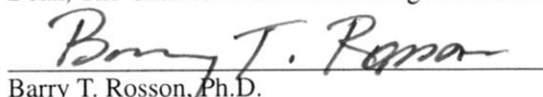
Warner Miller, Ph.D.

Chair, Department of Physics



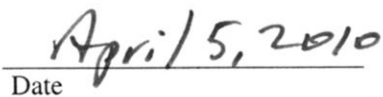
Gary W. Perry, Ph.D.

Dean, The Charles E. Schmidt College of Science



Barry T. Rosson, Ph.D.

Dean, Graduate College



Date

ACKNOWLEDGEMENTS

I am deeply thankful to my thesis advisor, Dr. Armin Fuchs, for giving me an opportunity to learn from him, for the enormous support and amount of time donated, for his ability to teach at different levels, for always being helpful, for making me want to learn more, for his professionalism and friendship.

I am grateful to my committee members Dr. Warner Miller, Dr. Scott Kelso, Dr. Viktor Jirsa and Dr. Douglas Cheyne for providing me with valuable feedback, and I greatly appreciate financial support for this work by NINDS (grant 48299, Scott Kelso, P.I.).

I thank my teachers, Prof. Oleg Kirillovich Sliva, Dr. Stephen Bruenn, Dr. Shen Li Qiu, Dr. Luc T. Wille and Dr. Sam Faulkner for sharing their knowledge with me.

I thank everybody at Physics Department and Center for Complex Systems and Brain Sciences for their support and helpful discussions.

I also extend my gratitude to my friends Ron and Sheila, my parents Lubov and Leonid, my brother Alexei for their love and support.

And last but definitely not least, I thank my family, my wife Olesya and daughter Emma for always being next to me when I needed it the most.

ABSTRACT

Author: Vyacheslav Murzin
Title: Detecting the Spatiotemporal Dynamics of Neural Activity on the Cortical Surface: Applying Anatomically Constrained Beamforming to EEG
Intitution: Florida Atlantic University
Dissertation Advisor: Dr. Armin Fuchs
Degree: Doctor of Philosophy
Year: 2010

The neurophysiological signals that are recorded in EEG (electroencephalography) and MEG (magnetoencephalography) originate from current flow perpendicular to the cortical surface due to the columnar organization of pyramidal cells in the cortical gray matter. These locations and directions have been used as anatomical constraints for dipolar sources in estimations of neural activity from MEG recordings. Here we extend anatomically constrained beamforming to EEG, which requires a more sophisticated forward model than MEG due to the blurring of the electric potential at tissue boundaries, but in contrast to MEG, EEG can account for both tangential and radial sources. Using computed tomography (CT) scans we create a realistic three-layer head model consisting of tessellated surfaces representing the tissue boundaries cerebrospinal fluid-skull, skull-scalp and scalp-air. The cortical gray matter surface, the anatomical constraint for the source dipoles, is extracted from magnetic resonance imaging (MRI) scans. EEG beamforming is implemented in a set of simulated data and compared for three different head models: single sphere, multi-

shell sphere and realistic geometry multi-shell model that employs a boundary element method. Beamformer performance is also analyzed and evaluated for multiple dipoles and extended sources (patches). We show that using anatomical constraints with the beamforming algorithm greatly reduces computation time while increasing the spatial accuracy of the reconstructed sources of neural activity. Using the spatial Laplacian instead of the electric potential in combination with beamforming further improves the spatial resolution and allows for the detection of highly correlated sources.

To my father, who used to say: "Physical work is the best relaxation for the brain."

Contents

| | |
|---|-------------|
| List of Figures | viii |
| 1 Introduction | 1 |
| 2 Source Localization | 5 |
| 2.1 Inverse Problem and Forward Solutions | 5 |
| 2.2 MEG Forward Solution | 6 |
| 2.3 EEG Forward Solution | 8 |
| 2.3.1 Single spherical conductor | 8 |
| 2.3.2 Multi-sphere case | 8 |
| 2.3.3 Multi-shell case (realistic geometry) | 10 |
| 2.4 Surface Laplacian | 13 |
| 2.5 Complementary Nature of EEG and MEG | 17 |
| 3 Beamforming | 19 |
| 3.1 What is a Beamformer? | 19 |
| 3.2 Linearly Constrained Minimum Variance Beamforming | 20 |
| 3.3 Invertibility of the Covariance Matrix | 22 |
| 4 Anatomical Constraints and Realistic Head Geometry | 23 |
| 4.1 Head Model: The Need for Realistic Geometry | 23 |
| 4.2 Extracting the Brain Surface: Freesurfer | 24 |

| | | |
|----------|--|-----------|
| 4.3 | Extracting Skull and Scalp Surfaces | 24 |
| 5 | Beamforming Simulations | 28 |
| 5.1 | EEG and MEG Data Sets | 28 |
| 5.2 | Realistic versus Spherical Head Models | 31 |
| 5.3 | Single Dipole Source Current | 33 |
| 5.4 | Two Dipole Source Currents | 37 |
| 5.5 | Three-Source Beamforming Simulation | 40 |
| 5.6 | Extended Sources | 41 |
| 5.7 | EEG versus MEG: Radial Sources | 43 |
| 5.8 | Correlated Sources: Surface Laplacian | 44 |
| 5.9 | Summary of the EEG Beamforming Simulations | 48 |
| 6 | Conclusions and Outlook | 51 |
| | Bibliography | 54 |

List of Figures

| | | |
|-----|--|----|
| 2.1 | Geometry of sensor and source. | 7 |
| 2.2 | Arbitrarily shaped multi-shell surfaces are implemented in the boundary element method. | 10 |
| 2.3 | Electric potential calculated on the different surfaces using the boundary element method. | 13 |
| 2.4 | Surface Laplacian derived from the electric potential on the scalp. . . | 16 |
| 2.5 | Dipoles representing neural activity sources are assumed to be located on the cortical surface with the direction perpendicular to the surface | 18 |
| 2.6 | MEG and EEG forward solution magnitudes plotted on the cortical surface. | 18 |
| 4.1 | Gray-white matter boundary surface extracted from an MRI scan using Freesurfer. | 25 |
| 4.2 | MRI scan versus CT scan. | 26 |
| 4.3 | Head surfaces extracted from a CT-scan. | 27 |
| 5.1 | EEG and MEG sensor locations and examples of forward solutions. . | 29 |
| 5.2 | A simulated EEG data set using two dipoles as main sources of neural activity. | 30 |
| 5.3 | Electric potential and corresponding magnetic field patterns: single dipole source in the left hemisphere | 32 |
| 5.4 | EEG forward solutions comparison for different head models with a dipolar current source in the left hemisphere. | 34 |
| 5.5 | Comparison of the electric activity detected from a single source when spherical and realistic geometry forward solutions are used. | 34 |

| | | |
|------|---|----|
| 5.6 | Simulated EEG patterns: single dipole source. | 35 |
| 5.7 | Beamforming activity index: single dipole source. | 35 |
| 5.8 | Simulated EEG patterns: two spatially distant dipole sources. | 38 |
| 5.9 | Beamforming activity index: two spatially distant dipole sources. | 38 |
| 5.10 | Simulated EEG patterns: two spatially close dipole sources. | 39 |
| 5.11 | Beamforming activity index: two spatially close dipole sources. | 39 |
| 5.12 | Beamforming activity index: three dipole sources. | 40 |
| 5.13 | Beamforming activity index: a single patch of nine dipoles with the same time series. | 41 |
| 5.14 | Beamforming activity index: two patches of nine source dipoles. | 42 |
| 5.15 | Beamforming activity index: MEG beamforming versus EEG beamforming. | 43 |
| 5.16 | Simulated EEG data set and corresponding surface Laplacian: binaural stimulus | 45 |
| 5.17 | Beamforming activity index calculated from the EEG forward solution. | 47 |
| 5.18 | Beamforming activity index calculated using the surface Laplacian derived from the EEG forward solution. | 47 |
| 5.19 | Beamforming activity index and reconstructed time courses calculated using surface Laplacian from two subsets of EEG sensors. | 48 |

Chapter 1

Introduction

Non-invasive recording techniques like Electroencephalography (EEG), Magnetoencephalography (MEG), Magnetic Resonance Imaging (MRI), functional MRI (fMRI), Positron Emission Tomography (PET) and Computed Tomography (CT) are of great importance as they provide complementary measures on structure and function of the living brain, essential for scientific research as well as clinical diagnostics. The zoo of imaging technologies is based on different physical principles and uses different tissue properties and physiological responses to operate. In CT and PET scans, the brain tissue is exposed to hard radiation in the form of X-rays and γ -photons, respectively, where, in the case of PET, radioactive glucose molecules have to be injected into the bloodstream. The exposure of biological tissue to this kind of radiation causes damage and therefore CT and PET are better classified as mildly-invasive than non-invasive and there are restrictions for using them in research with healthy human subjects.

MRI and fMRI measure the level of water and the hemodynamic response (changes in blood flow and level of oxygen in the blood induced by a certain task), respectively [Howseman, Bowtell, 1999]. The neural sources in the brain produce electric currents, whose effects can be measured in the form of magnetic fields outside the head or electric potentials on the scalp surface using MEG or EEG. These measurements have the common primary goal of estimating the locations of neural activity in the brain.

fMRI, when compared to M/EEG, offers real 3-D imaging with the highest spatial resolution of source localization (as high as 1-3 mm) [Baillet et al., 2001], but due to the nature of the hemodynamic response has very limited temporal resolution, being able to detect brain activity on a scale of seconds. In contrast, M/EEG equipment typically measures changes in electric and magnetic fields with a sampling rate of 1000 Hz whereas most of the brain activity ranges from 0.1 to 100 Hz and is well within the ranges detectable with M/EEG. The main problem is to find the locations and directions of the neural sources inside the brain from electric potentials or magnetic fields measured on the outside of the head. This so-called inverse problem cannot be solved uniquely [von Helmholtz, 1853] because there can be infinitely many source configurations leading to the same potential or magnetic field readings at the sensors.

Various approaches have been developed to obtain inverse solutions by means of estimating neural activity from M/EEG measurements. These include minimum norm estimation [Gorodnitsky et al., 1992; Koles, 1998; Liu et al., 1998], dipole source analysis/localization (DSL), which is implemented in commercially available software packages like BESA and EMSE, multiple signal classification (MUSIC) [Schmidt, 1986; Moshier, et al., 1992], independent component analysis (ICA) [Delorme, Makeig, 2004], lead-field-based imaging [Hämäläinen, Ilmoniemi, 1994], beamforming [van Veen et al., 1997; Robinson, Vrba, 1999], etc.

Beamforming is a signal processing technique that is based on the calculation of the covariance between signals at different sensors, such that they are most sensitive to a certain location and direction inside a volume while at the same time suppressing interference from all other locations. Beamforming was initially developed as an application with radio and sound waves [Frost, 1972; Borgiotti, Kaplan, 1979] and later used in MEG source localization [van Veen, Buckley, 1988; Sekihara, 1996; Robinson, Vrba, 1999; Cheyne, Gaetz, 2003; Cheyne et al., 2006]. Applications of

beamforming to EEG have also been reported [Spencer et al., 1992; Ward et al., 1998; van Hoey et al., 1999; Brookes et al., 2008; Wong, Gordon, 2009] but it appears that to this day anatomically constrained beamforming, based on realistic geometry forward solution, has not been applied to EEG.

Beamforming methods have certain advantages with respect to other source localization techniques. In contrast to dipole source localization, beamforming does not require a priori assumption of the number of active sources and is capable of dealing with distributed sources [van Veen et al., 1997]. Beamforming also has advantages over minimum-norm solutions, which have low spatial resolution and a tendency to overestimate superficial sources compared to deeper ones [Lin et al., 2006]. Beamforming can deal with spatially close or deep sources and under favorable signal-to-noise ratios reaches the spatial resolution of the minimum size of the grid [Hillebrand, Barnes, 2003]. The main problem in beamforming is its poor performance in the presence of highly correlated sources, such as bilateral activation during binaural stimulation, in particular with MEG [Brookes et al., 2008; Dalal et al., 2006; Popescu et al., 2008]. In the present study a novel method of detecting correlated sources in EEG is suggested.

Originally, beamforming was developed to scan the whole brain or a region of interest on a grid of a certain size, where the sources were assumed to be at the nodes of the grid, leading to a 5 degree of freedom task: 3 degrees for the location and 2 for the direction of the source. This dimensionality can be significantly reduced if anatomical constraints are taken into account. It is well known that the signals picked up by EEG or MEG can only be produced by simultaneous activation of tens of thousands of neurons [Nunez, Srinivasan, 2006] acting coherently as in the cortical gray matter [Braitenberg, Schüz, 1991]. Furthermore, the structure of the pyramidal cells in the gray matter suggests that the cell bundles, known as macrocolumns, are

oriented perpendicularly to the surface. Taking these facts together, anatomically constrained beamforming assumes all sources confined to the cortical surface with the direction perpendicular to the surface.

This thesis has the following layout. In Chapter 2, the electromagnetic inverse problem is described and types of forward solutions available for comparison are shown. Chapter 3 provides insights into the beamforming algorithm, namely the linearly constrained minimum variance (LCMV) beamformer and how its weights and activity index are calculated. Chapter 4 discusses the head surfaces that are extracted from CT and MRI scans and how these surfaces are implemented in beamforming. The simulation results are presented in Chapter 5. It is demonstrated how using the realistic geometry head model instead of the spherical models improves spatial resolution of the source localization. The beamforming is applied to different source configurations: single dipole, two and three dipoles and extended sources (patches). At the final stage of simulations, it is shown how the surface Laplacian allows for detection of temporally highly correlated sources.

Source Localization

2.1 Inverse Problem and Forward Solutions

Neuronal cells when activated by an external input generate tiny electric currents, which also generate magnetic fields, but in order to be measurable from the outside of the head, several thousands of neighboring neurons must act coherently with current flow in the same direction. Pyramidal cells in gray matter, which are densely populated and organized in macrocolumns perpendicular to the cortical surface, are commonly accepted as the main generators of the EEG and MEG signals. Estimates of the underlying neural activity from surface readings of scalp potentials in EEG or magnetic fields in MEG are known as an inverse problem. This problem is ill-posed because the number of EEG and/or MEG sensors is much smaller than the number of unknown sources and there is also an infinite number of source configurations that do not produce a signal on the outside of the volume. Thus, the inverse problem in electromagnetic fields cannot be solved directly although methods exist that allow for the localization of neuronal activity with fairly good resolution. One way to approach the inverse problem is to use so-called beamforming, which requires computation of the forward solution.

An electromagnetic forward solution assumes a current dipole (or a finite set of them) inside a volume and provides the electric potential and/or magnetic field

strength at points of interest (sensors) and will be denoted by \mathbf{G} . The magnetic field \mathbf{B} is not affected when penetrating head tissues (as their relative permeability is $\mu/\mu_0 \cong 1$) and can be modeled fairly easily. In contrast, the propagation of the electrostatic field is greatly reduced and smeared out at the boundaries of tissues with different conductivities. The skull conductivity is about 100 times smaller than the conductivity of the cerebro-spinal fluid (CSF) and skin, and therefore cannot be neglected when modeling the EEG forward solution. We shall compare three different head models: the single homogeneous sphere of constant conductivity, a more realistic 3-layer concentric sphere model where the conductivity of each layer is taken into account and a 3-layer model that is not restricted to the spherical shape and utilizes the real geometry of the head created from CT and MRI scans of the subject.

2.2 MEG Forward Solution

Assuming the time derivatives of the electric and magnetic fields corresponding to the biological signals measured in EEG and MEG are sufficiently small, they can be neglected in Maxwell's equations [Plonsey, Heppner, 1967], leading to the quasi-static approximation for the magnetic field

$$\nabla \times \mathbf{B}(\mathbf{r}) = \mu_0 \mathbf{j}(\mathbf{r}) \quad \text{and} \quad \nabla \cdot \mathbf{B}(\mathbf{r}) = 0 \quad (2.1)$$

The curl of the magnetic field at location \mathbf{r} is proportional to the current density and the divergence of the magnetic field is zero. The field produced by a current in a closed volume Γ of finite conductivity is given by the integral form of the Biot-Savart law [Mosher et al., 1999]

$$\mathbf{B}(\mathbf{r}) = \frac{\mu_0}{4\pi} \int_{\Gamma} \mathbf{j}(\mathbf{r}_q) \times \mathbf{d}/d^3 d\mathbf{r}_q \quad (2.2)$$

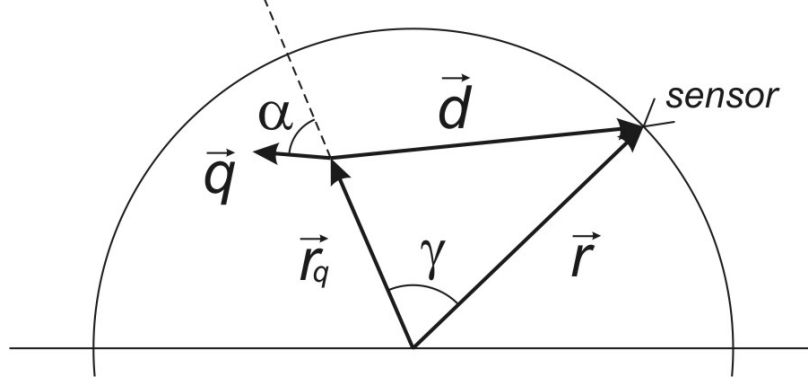


Figure 2.1: Geometry of sensor and source: the source \mathbf{q} is located at \mathbf{r}_q , the sensor is at \mathbf{r} . The angle between \mathbf{q} and \mathbf{r}_q is denoted as α , the angle between \mathbf{r} and \mathbf{r}_q as γ and the angle between the planes formed by $(\mathbf{r}, \mathbf{r}_q)$ and $(\mathbf{q}, \mathbf{r}_q)$ is denoted as β (not shown). The vector from the dipole to the sensor is \mathbf{d} .

where $\mathbf{j}(\mathbf{r}_q)$ is the current density at \mathbf{r}_q , and $\mathbf{d} = \mathbf{r} - \mathbf{r}_q$ (with magnitude d) is the distance between the observation point \mathbf{r} and the source point \mathbf{r}_q as shown in Figure 2.1. For locations outside a spherical conductor the magnetic field can be calculated according to Sarvas [Sarvas, 1987]

$$\mathbf{B}(\mathbf{r}) = \frac{\mu_0}{4\pi F^2(\mathbf{r}, \mathbf{r}_q)} \{F(\mathbf{r}, \mathbf{r}_q) \mathbf{q} \times \mathbf{r}_q - [\mathbf{q} \times \mathbf{r}_q \cdot \mathbf{r}] \nabla F(\mathbf{r}, \mathbf{r}_q)\} \quad (2.3)$$

where the scalar function $F(\mathbf{r}, \mathbf{r}_q)$ and its gradient $\nabla F(\mathbf{r}, \mathbf{r}_q)$ are given by

$$F(\mathbf{r}, \mathbf{r}_q) = d(rd + r^2 - \mathbf{r}_q \cdot \mathbf{r}) \quad (2.4)$$

$$\nabla F(\mathbf{r}, \mathbf{r}_q) = \left(\frac{d^2}{r} + \frac{\mathbf{d} \cdot \mathbf{r}}{d} + 2d + 2r \right) \mathbf{r} - \left(d + 2r + \frac{\mathbf{d} \cdot \mathbf{r}}{d} \right) \mathbf{r}_q \quad (2.5)$$

It is commonly known that MEG is virtually blind to radial sources in spherical conductors, due to field cancellation by secondary currents, and most sensitive to the tangential sources located in the walls of cortical sulci. As can be seen, Sarvas' formula (2.3) contains two cross-products $\mathbf{q} \times \mathbf{r}_q$, leading to $\mathbf{B}(\mathbf{r}) = \mathbf{0}$ for a perfectly radial source ($\mathbf{q} \parallel \mathbf{r}_q$) in a spherical conductor independent of sensor and source location.

2.3 EEG Forward Solution

2.3.1 Single spherical conductor

When an electric current is inside a conducting volume, the potential that arises on the surface depends on the shape of the volume and its conductivity. The first and simplest model of the human head is to approximate it by a single sphere of constant conductivity.

The source current is represented by a vector \mathbf{q} located at \mathbf{r}_q as shown in Figure 2.1. The conductor is a sphere of radius r and constant conductivity σ . The electric potential on the scalp at the sensor location, represented by vector \mathbf{r} , in this case can be expressed in closed form [Mosher et al., 1999]

$$\begin{aligned} V_s(\mathbf{r}, \mathbf{r}_q, \mathbf{q}) = & \frac{q \cos \alpha}{4\pi\sigma} \left(\frac{2(r \cos \gamma - r_q)}{d^3} + \frac{1}{r_q d} - \frac{1}{r r_q} \right) \\ & + \frac{q \sin \alpha}{4\pi\sigma} \cos \beta \sin \gamma \left(\frac{2r}{d^3} + \frac{d+r}{r d (r - r_q \cos \gamma + d)} \right) \end{aligned} \quad (2.6)$$

where the radius of the sphere is $r = |\mathbf{r}|$, the distance between the sensor and the dipole location is $d = |\mathbf{r} - \mathbf{r}_q|$ and the angles α , β and γ are as defined in Figure 2.1.

Equation (2.6) shows that the potential on the surface of a spherical conductor can be determined as a function of the sensor and source locations (and angles between the corresponding vectors), and the conductivity of the medium. This model is simple and fast to calculate but it is not able to provide an accurate forward solution for EEG, since it does not take different tissue conductivities and head shape into account.

2.3.2 Multi-sphere case

The conductivity of the skull is about 100 times less than the conductivity of the brain and one way to model the head is to consider the brain as a spherical conductor, surrounded by two concentric spherical shells, representing the skull and scalp. This

so-called multi-spherical forward solution takes differences in conductivities of the head tissues into account and requires the evaluation of an infinite sum [Zhang, 1995].

The potential on the outermost (m^{th}) surface then reads

$$V_m(\mathbf{r}, \mathbf{r}_q, \mathbf{q}) = \frac{q}{4\pi\sigma_m r^2} \sum_{n=1}^{\infty} \frac{2n+1}{n} \left(\frac{r_q}{r}\right)^{n-1} f_n \times \{n \cos \alpha P_n(\cos \gamma) + \cos \beta \sin \alpha P_n^1(\cos \gamma)\} \quad (2.7)$$

where P_n and P_n^1 are the Legendre and associated Legendre polynomials, respectively, and

$$f_n = \frac{n}{m_{22} + (1+n)m_{21}} \quad (2.8)$$

The coefficients m_{22} and m_{21} are found from

$$M = \begin{pmatrix} m_{11} & m_{12} \\ m_{21} & m_{22} \end{pmatrix} = \frac{1}{(2n+1)^{M-1}} \times \prod_{k=1}^{m-1} \begin{pmatrix} n + \frac{(n+1)\sigma_k}{\sigma_{k+1}} & (n+1) \left(\frac{\sigma_k}{\sigma_{k+1}} - 1\right) \left(\frac{r_q}{r_k}\right)^{2n+1} \\ n \left(\frac{\sigma_k}{\sigma_{k+1}} - 1\right) \left(\frac{r_k}{r_q}\right)^{2n+1} & (n+1) + \frac{n\sigma_k}{\sigma_{k+1}} \end{pmatrix} \quad (2.9)$$

In numerical calculations the infinite series (2.7) was found to converge before $n=20$ and was truncated at this point. It must be noted that the matrices in (2.9) are non-commuting and the matrix with the highest index number is to be applied first, e.g. on the leftmost side. The most commonly used spherical multi-shell head model includes three layers: cerebrospinal fluid (CSF), skull and scalp, which leads to $m = 3$. For our simulations the values for the conductivities of the CSF and scalp layers were chosen to be $\sigma_1 = \sigma_3 = 1.0$ and conductivity of the skull $\sigma_2 = 0.01$.

The multi-shell model is still restricted by the unrealistic assumption of spherical surfaces for the layer boundaries. It is possible to consider ellipsoidal approximations, etc., but ultimately the most accurate method is to use a realistic model derived from

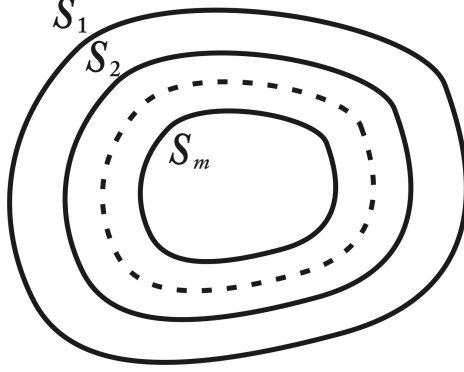


Figure 2.2: Arbitrarily shaped multi-shell surfaces are implemented in the boundary element method. The surfaces are labeled from 1 (outermost) to m (innermost).

a real human head. This model takes into account not only the different tissue layers but also these layers' shape and thickness in different regions of the head.

2.3.3 Multi-shell case (realistic geometry)

The interfaces between the regions of different conductivity, as shown in Figure 2.2, will be denoted by S_1, \dots, S_m , with S_1 circumventing all the remaining surfaces, i.e. S_1 is the scalp. It can be shown that the electric potential V at $\mathbf{r} \in S_i$ obeys the Fredholm integral equation [Mosher et al., 1999]

$$(\sigma_i^- + \sigma_i^+)V(\mathbf{r}) = 2V_0(\mathbf{r}) + \frac{1}{2\pi} \sum_{j=1}^m (\sigma_j^- - \sigma_j^+) \int V(\mathbf{r}') d\Omega_{\mathbf{r}}(\mathbf{r}') \quad (2.10)$$

Here the conductivities inside and outside the surface S_j are denoted by σ_j^- and σ_j^+ , respectively. The solid angle $d\Omega_{\mathbf{r}}(\mathbf{r}')$ subtended at the location \mathbf{r} by a surface element $d\mathbf{S}$ at \mathbf{r}' is given by

$$d\Omega_{\mathbf{r}}(\mathbf{r}') = \frac{(\mathbf{r}' - \mathbf{r})}{|\mathbf{r}' - \mathbf{r}|^3} \cdot d\mathbf{S}_j(\mathbf{r}')$$

and

$$V_0(\mathbf{r}) = \frac{1}{4\pi\sigma_0} \int d^3r' \frac{\nabla' \cdot \mathbf{j}(\mathbf{r}')}{|\mathbf{r}' - \mathbf{r}|}$$

is the potential caused by the current source \mathbf{j} in an infinite homogeneous medium with conductivity $\sigma = 1$. To solve (2.10) numerically, the surfaces S_i are divided into triangles Δ_k^i , resulting in a set of linear equations

$$\mathbf{V}^i = \sum_{j=1}^m \mathbf{B}^{ij} \mathbf{V}^j + \mathbf{g}^i; \quad i = 1, \dots, m \quad (2.11)$$

where the matrices \mathbf{V}^i , \mathbf{g}^i and \mathbf{B}^{ij} are defined by

$$\begin{aligned} V_k^i &= \frac{1}{\mu_k^i} \int_{\Delta_k^i} V(\mathbf{r}) dS_i \\ g_k^i &= \frac{1}{\mu_k^i} \frac{2}{\sigma_i^- + \sigma_i^+} \int_{\Delta_k^i} V_0(\mathbf{r}) dS_i \\ B_{kl}^{ij} &= \frac{1}{2\pi} \frac{1}{\mu_k^i} \Gamma_{ij} \int_{\Delta_k^i} \Omega_{\Delta_l^j}(\mathbf{r}) dS_i \end{aligned} \quad (2.12)$$

Here i and j are the index numbers of the surfaces, and k and l are the index numbers of the triangles on the surfaces. In addition, μ_k^i is the area of the k^{th} triangle Δ_k^i on the surface S_i and $\Omega_{\Delta_l^j}$ is the solid angle subtended by the triangle Δ_l^j at the position of the center of the triangle Δ_k^i . For $k = l$ and $i = j$, $\Omega_{\Delta_l^j} = 0$. The number of triangles on each surface S_j is denoted by n_j and $\sum_{j=1}^m n_j = N$. The multipliers Γ_{ij} are given by

$$\Gamma_{ij} = \frac{\sigma_j^- - \sigma_j^+}{\sigma_i^- + \sigma_i^+} \quad (2.13)$$

We consider a three-layer head model with surfaces S_i , where $i = 1$ for the scalp, $i = 2$ for the skull and $i = 3$ for the cerebrospinal fluid/brain. The coefficients B_{kl}^{ij} in (2.12) can be calculated using the solid angle of a plane triangle [van Oosterom, Strackee, 1983]

$$\Omega_{\Delta_l^j}(\mathbf{r}_{c_k^i}) = \frac{2\mathbf{R}_1 \cdot (\mathbf{R}_2 \times \mathbf{R}_3)}{R_1 R_2 R_3 + (\mathbf{R}_1 \cdot \mathbf{R}_2) R_3 + (\mathbf{R}_1 \cdot \mathbf{R}_3) R_2 + (\mathbf{R}_2 \cdot \mathbf{R}_3) R_1} \quad (2.14)$$

with $R_i = |\mathbf{R}_i|$. The source g_k^i in (2.11) is defined by the dipole

$$g_k^i = \frac{1}{2\pi(\sigma_i^- + \sigma_i^+)} \sum_{r'} \frac{\nabla' \cdot \mathbf{j}(\mathbf{r}')}{|\mathbf{r} - \mathbf{r}'|} \quad (2.15)$$

The solution of (2.10) in the case of three surface layers can be represented by

$$\mathbf{V} = \begin{pmatrix} \mathbf{V}^1 \\ \mathbf{V}^2 \\ \mathbf{V}^3 \end{pmatrix} = \begin{pmatrix} \mathbf{W}^1 \\ \mathbf{W}^2 \\ \mathbf{W}^3 + \mathbf{W}_0^3 \end{pmatrix} \quad (2.16)$$

where the term \mathbf{W}_0^3 has been added to avoid numerical problems and represents the potential on the surface of a homogeneous conductor bounded by surface S_3 [Hämäläinen, Sarvas, 1989]

$$\mathbf{W}_0^3 = \left(\frac{\mathbf{B}^{33}}{\Gamma^{33}} - \frac{1}{n_3} \right) \mathbf{W}_0^3 + \frac{\sigma_3^- + \sigma_3^+}{\sigma_3^-} \mathbf{g}^3 \quad (2.17)$$

The unknown functions \mathbf{W}^i can be found by solving the system of linear equations

$$\mathbf{W} = \begin{pmatrix} \mathbf{W}^1 \\ \mathbf{W}^2 \\ \mathbf{W}^3 \end{pmatrix} = \left(\mathbf{B}^{ij} - \frac{1}{n_1 + n_2 + n_3} \right) \mathbf{W} + \sigma_3^+ \begin{pmatrix} \mathbf{h}^1 \\ \mathbf{h}^2 \\ \mathbf{h}^3 \end{pmatrix} \quad (2.18)$$

where

$$\mathbf{h}^1 = \frac{\mathbf{g}^1}{\sigma_3^-} \quad \mathbf{h}^2 = \frac{\mathbf{g}^2}{\sigma_3^-} \quad \mathbf{h}^3 = \frac{\mathbf{g}^3}{\sigma_3^-} - \frac{2}{\sigma_3^- + \sigma_3^+} \mathbf{W}_0^3$$

To solve (2.17) for \mathbf{W}_0^3 , we rewrite it in the form

$$\left\{ \mathbf{I} - \frac{\mathbf{B}^{33}}{\Gamma^{33}} + \frac{1}{n_3} \right\} \mathbf{W}_0^3 = \frac{\sigma_3^- + \sigma_3^+}{\sigma_3^-} \mathbf{g}^3 \quad (2.20)$$

where \mathbf{I} is the identity matrix and the scalar $\frac{1}{n_3}$ is added to all elements of $\mathbf{I} - \frac{\mathbf{B}^{33}}{\Gamma^{33}}$.

The solution of this system of linear equations together with the set of equations (2.18) is then used to find the unknown vector \mathbf{W}

$$\left\{ \mathbf{I} - \mathbf{B}^{ij} + \frac{1}{n_1 + n_2 + n_3} \right\} \mathbf{W} = \sigma_3^+ \mathbf{h} \quad (2.21)$$

Numerical calculations start with the geometry matrix \mathbf{B}^{ij} in (2.12). The time to calculate this matrix depends on the number of vertices in the tessellation and can be computationally expensive but it has to be performed only once per subject. Then

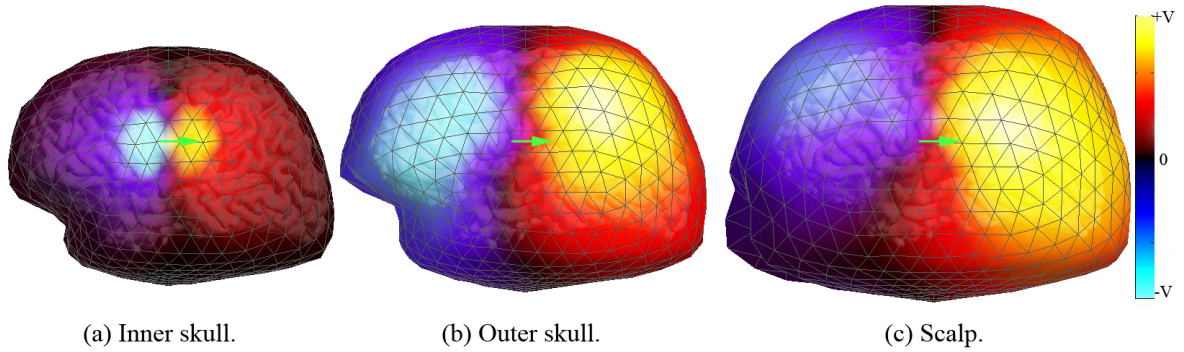


Figure 2.3: Electric potential calculated on the different surfaces using the boundary element method for a single source located in the left hemisphere with direction anterior to posterior: (a) interface between cerebrospinal fluid and skull, (b) interface between skull and scalp, (c) interface between scalp and air. The blurring and attenuation of the electric potential happens primarily in the skull. Yellow: positive potential, blue: negative potential.

a source dipole is placed inside the innermost volume and the potential on all three surfaces is calculated using (2.16). One of the advantages of the boundary element method is that one obtains the distribution of the electric potential on all three surfaces, i.e. \mathbf{V}_1 , \mathbf{V}_2 and \mathbf{V}_3 , and can actually visualize how the potential blurs and smears out as it penetrates through skull and scalp. The example in Figure 2.3 shows the electric potential for a single source located in the left hemisphere with direction anterior to posterior. The potential distribution is fairly localized on the boundary between the cerebrospinal fluid and skull. As the potential travels through the skull, it gets blurred, scattered and attenuated, and when it finally arrives at the scalp surface it is even more smeared out and attenuated.

2.4 Surface Laplacian

EEG measurements are known to produce blurry images due to low skull conductivity, greatly affecting the overall accuracy of source reconstruction. One way to deal with

this problem is to calculate the surface Laplacian or second spatial derivative of the scalp potential with respect to the two surface coordinates [Gevins, 1989; Nunez, Srinivasan, 2006]. The physical meaning of the surface Laplacian can be derived starting from the general form of Maxwell's equations for the electric field \mathbf{E} and magnetic field \mathbf{B}

$$\begin{aligned} \text{curl } \mathbf{E} &= -\frac{1}{c} \frac{\partial \mathbf{B}}{\partial t} & \text{curl } \mathbf{B} &= \frac{1}{c} \frac{\partial \mathbf{E}}{\partial t} + \frac{4\pi}{c} \mathbf{j} \\ \text{div } \mathbf{E} &= 4\pi\rho & \text{div } \mathbf{B} &= 0 \end{aligned} \quad (2.22)$$

where \mathbf{j} is the current density and ρ is the electric charge density. Assuming that the electromagnetic fields are changing slowly ($f < 10^2$ Hz), so that the time-derivatives in (2.22) are negligible¹, we obtain the quasi-static approximation

$$\begin{aligned} \text{curl } \mathbf{E} &= \mathbf{0} & \text{curl } \mathbf{B} &= \frac{4\pi}{c} \mathbf{j} \\ \text{div } \mathbf{E} &= 4\pi\rho & \text{div } \mathbf{B} &= 0 \end{aligned} \quad (2.23)$$

As the curl of the electric field vanishes, \mathbf{E} can be written as the negative gradient of a potential function ϕ

$$\mathbf{E} = -\text{grad } \phi = -\nabla \phi \quad (2.24)$$

which leads to

$$\nabla \times \nabla \phi = \mathbf{0} \quad \text{and} \quad \nabla \cdot \nabla \phi = -4\pi\rho \quad (2.25)$$

where $\nabla \cdot \nabla \phi = \Delta\phi$ is the Laplacian of the potential. The second equation in (2.25) is the well-known Poisson equation

$$\Delta\phi(x, y, z) = -4\pi\rho(x, y, z) \quad (2.26)$$

which states that the Laplacian of the electric potential at every point in space is proportional to the electric charge density at this point. This means that the Laplacian is a physical quantity in contrast to the electric potential, which depends on

¹This assumption is valid if the propagation, capacitive and inductive effects are neglected and the boundary conditions are stationary [Plonsey, Heppner, 1967].

the reference used. Now we consider the three-dimensional Laplacian in spherical coordinates

$$\Delta\phi(r, \theta, \varphi) = \frac{1}{r^2} \left[\frac{\partial}{\partial r} \left(r^2 \frac{\partial\phi}{\partial r} \right) + \frac{1}{\sin\theta} \frac{\partial}{\partial\theta} \left(\sin\theta \frac{\partial\phi}{\partial\theta} \right) + \frac{1}{\sin^2\theta} \frac{\partial^2\phi}{\partial\varphi^2} \right]$$

where we can distinguish between the first term inside the square brackets as the radial part Δ_r and the other two terms as the tangential part $\Delta_{\theta\varphi}$

$$\Delta\phi(r, \theta, \varphi) = \Delta_r\phi + \Delta_{\theta\varphi}\phi = -4\pi\rho(r, \theta, \varphi) \quad (2.27)$$

Since there is no free charge on the surface of the conducting volume (scalp), the charge density $\rho(r, \theta, \varphi)$ vanishes and it follows

$$\rho(r, \theta, \varphi) = 0 \quad \Rightarrow \quad \Delta_r\phi = -\Delta_{\theta\varphi}\phi \quad (2.28)$$

The tangential part of the Laplacian $\Delta_{\theta\varphi}\phi$ can be calculated from surface measurements of the electric potential and its radial part is given by

$$\Delta_r\phi = \frac{1}{r^2} \frac{\partial}{\partial r} \left(r^2 \frac{\partial\phi}{\partial r} \right) = \frac{1}{r^2} \left[2r \frac{\partial\phi}{\partial r} + r^2 \frac{\partial^2\phi}{\partial r^2} \right] = \frac{2}{r} \frac{\partial\phi}{\partial r} + \frac{\partial^2\phi}{\partial r^2} \quad (2.29)$$

The gradient of the potential in the radial direction $\frac{\partial\phi}{\partial r}$ is the radial part of the electric field E_r , and since the electric field, according to Ohm's law, is proportional to the current density ($\mathbf{j} = \sigma\mathbf{E}$), it follows that

$$\frac{\partial\phi}{\partial r} \sim j_r \quad (2.30)$$

The second derivative $\frac{\partial^2\phi}{\partial r^2}$ in (2.29) can be neglected due to the fact that the electric potential in a homogeneous conductor falls off linearly, leading to

$$\Delta_r\phi \sim j_r \quad (2.31)$$

i.e. the radial part of the Laplacian is proportional to the radial component of the

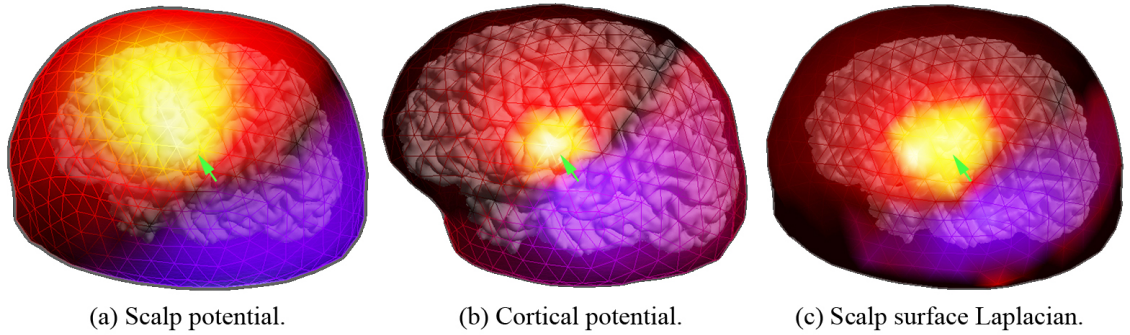


Figure 2.4: Surface Laplacian derived from the electric potential on the scalp is an estimate of the electric current density or cortical potential. (a) Electric potential on the scalp surface from a single source dipole, located in the left primary auditory cortex, (b) electric potential on the CSF surface from the same source, (c) negative of the surface Laplacian calculated from (a).

current density, which represents currents entering or leaving the surface of the scalp (current sources and sinks). Figure 2.4 shows a comparison between the negative of the surface Laplacian, and the electric potential (forward solution) calculated on the scalp (a) and on the cerebrospinal fluid (b), the latter representing the cortical potential. The surface Laplacian (c) is localized similarly to the cortical potential and can serve as its estimate. As it turns out, this property is advantageous in beamforming applications, in particular, if highly correlated sources are considered.

2.5 Complementary Nature of EEG and MEG

When the forward solution \mathbf{G} in EEG or MEG for a single dipole source is calculated, it is represented by the values of the magnetic field strength at the MEG coils or electric potential at the EEG sensors. These values at the sensors can be seen as a vector and the magnitude of this vector can be called a magnitude of a forward solution $|\mathbf{G}|$. Figure 2.5 shows a magnified segment of the cortical surface tessellation, in which every vertex represents the location of a dipole (green arrows) and the direction is perpendicular to the surface. The magnitude of a magnetic forward solution $|\mathbf{G}|$, calculated using the spherical model (2.3) for every point in the cortical surface tessellation is shown in Figure 2.6(a). The walls of sulci are red to bright yellow, representing high magnitudes of the forward solution. The values plotted in light blue are close to zero and correspond to locations that are deep inside the brain and to radial sources (top of gyri). This is due to the fact that the magnetic field from radial components of the dipole sources outside a spherical conductor is zero, as discussed in Chapter 2.2. In contrast, the electroencephalogram is sensitive to both radial and tangential sources as shown in Figure 2.6(b). Moreover, EEG is most sensitive to the radial sources located on top of the gyri, because these sources generate a stronger and more focused electric potential at the scalp. In this perspective, EEG and MEG offer complementary information about the sources of electromagnetic activity in the brain.

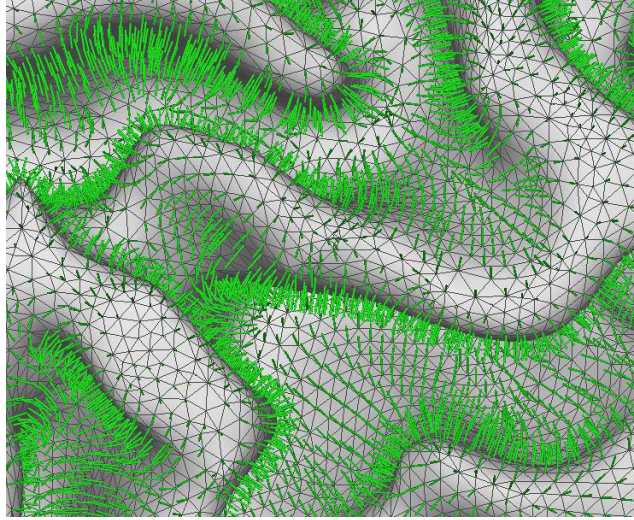
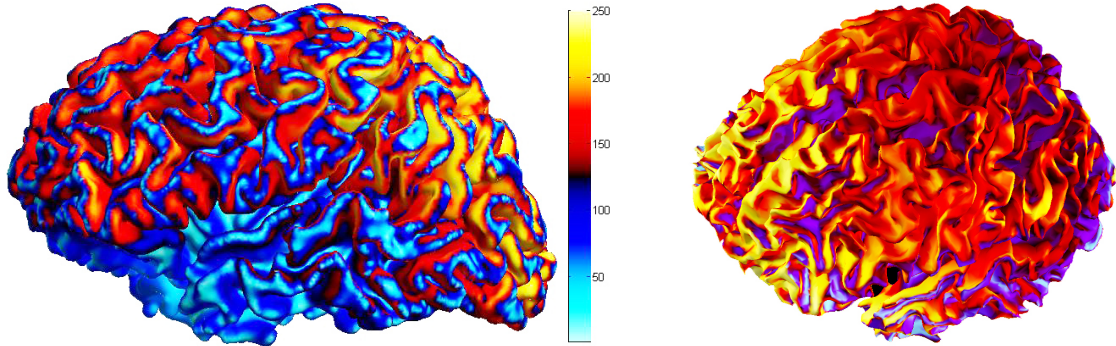


Figure 2.5: Dipoles representing neural activity sources are assumed to be located on the cortical surface with the direction perpendicular to the surface.



(a) MEG

(b) EEG

Figure 2.6: MEG and EEG forward solution magnitudes plotted on the cortical surface. Relative magnitudes depend on dipole source location and direction. Yellow indicates high values of magnitude, cyan indicates values close to zero.

Beamforming

3.1 What is a Beamformer?

Beamforming is a signal processing technique for sensor arrays that has been developed in various applications for sound and radio waves. In general, it may be viewed as a spatial filter that focuses an array of sensors onto a signal from a certain location while suppressing all other sources and interferences. There are two main types of beamformers: conventional and adaptive. Conventional (fixed or switched beam) beamformers use a fixed set of weights, usually based on the properties of the sensors. In contrast, adaptive beamformers combine these properties with the actual signals received by the sensors, which improves focusing on the point of interest and increases the signal-to-noise ratio.

For about a decade, adaptive beamformers have been applied to source localization in magnetoencephalography [Cheyne et al., 2006; Huang et al., 2004; Robinson, Vrba, 1999]. The so-called linearly constrained minimum variance (LCMV) beamformers are spatial filters that use linear weighting of the sensor channels to focus the array on a given target location. In our study, this method is applied to the EEG source localization problem.

3.2 Linearly Constrained Minimum Variance Beamforming

MEG or EEG data from an array of sensors or electrodes can be represented by a time dependent vector $\mathbf{X}(t)$. In LCMV beamforming, the signal $S_{\Theta}(t)$ measured by $\mathbf{X}(t)$ that originates from a source at Θ is given by $S_{\Theta}(t) = \mathbf{H}_{\Theta} \cdot \mathbf{X}(t)$ where $\Theta = (x, y, z, \psi, \phi)$ is a 5-dimensional quantity, which represents the location and direction of the current source, and \mathbf{H}_{Θ} are called the beamformer weights. The global source power originating from Θ reads

$$\begin{aligned}
 S_{\Theta}^2 &= \frac{1}{T} \int_0^T \{\mathbf{H}_{\Theta} \cdot \mathbf{X}(t)\}^2 dt \\
 &= \frac{1}{T} \int_0^T dt \left\{ \sum_{i=1}^M H_{\Theta i} X_i(t) \right\}^2 \\
 &= \sum_{i=1}^M \sum_{j=1}^M H_{\Theta i} H_{\Theta j} \underbrace{\frac{1}{T} \int_0^T X_i(t) X_j(t) dt}_{C_{ij}}
 \end{aligned} \tag{3.1}$$

where i, j represent the index number of a sensor and C_{ij} is the correlation matrix. Using \mathbf{C} , the global source power originating from Θ can be written in the compact form

$$S_{\Theta}^2 = \sum_{i=1}^M \sum_{j=1}^M C_{ij} H_{\Theta i} H_{\Theta j} = \mathbf{H}_{\Theta} \cdot \mathbf{C} \mathbf{H}_{\Theta} \tag{3.2}$$

The beamformer weights \mathbf{H}_{Θ} are determined such that the total power over a certain time span becomes a minimum under the constraint that the signal originating from Θ , the forward solution \mathbf{G}_{Θ} , remains constant, i.e.

$$S_{\Theta}^2 = \frac{1}{T} \int_0^T \{\mathbf{H}_{\Theta} \cdot \mathbf{X}(t)\}^2 dt = \mathbf{H}_{\Theta} \cdot \mathbf{C} \mathbf{H}_{\Theta} \rightarrow \min \tag{3.3}$$

with the constraint $S_{\Theta} = \mathbf{H}_{\Theta} \cdot \mathbf{G}_{\Theta} = 1$.

The problem (3.3) is solved using the method of Lagrange multipliers [van Veen et al., 1997], a well-known method from classical mechanics. The constraint is written as

$$\mathbf{H}_\Theta \cdot \mathbf{G}_\Theta - 1 = 0 \quad (3.4)$$

then multiplied by a constant λ and added to the global source power S_Θ^2

$$S_\Theta^2 = \sum_{i=1}^M \sum_{j=1}^M C_{ij} H_{\Theta i} H_{\Theta j} + \lambda \left\{ \sum_{i=1}^M H_{\Theta i} G_{\Theta i} - 1 \right\} \rightarrow \min \quad (3.5)$$

The source power is now minimized by taking the derivative of S_Θ^2 with respect to \mathbf{H}_Θ and solving

$$\frac{\partial S_\Theta}{\partial H_{\Theta k}} = 2 \sum_{i=1}^M C_{ik} H_{\Theta i} + \lambda G_{\Theta k} = 0 \quad (3.6)$$

for \mathbf{H}_Θ . Equation (3.6) in matrix form reads

$$2\mathbf{C}\mathbf{H}_\Theta = -\lambda\mathbf{G}_\Theta \quad (3.7)$$

from which it follows

$$\mathbf{H}_\Theta = -\frac{\lambda}{2}\mathbf{C}^{-1}\mathbf{G}_\Theta \quad (3.8)$$

The unknown Lagrange multiplier is found by using the constraint (3.4) again, leading to

$$\left[-\frac{\lambda}{2}\mathbf{C}^{-1}\mathbf{G}_\Theta \right] \cdot \mathbf{G}_\Theta = 1 \quad \text{or} \quad \lambda = -2 [\mathbf{G}_\Theta \cdot \mathbf{C}^{-1}\mathbf{G}_\Theta]^{-1} \quad (3.9)$$

Now (3.9) is inserted into the solution (3.8) and the beamformer coefficients are obtained

$$\mathbf{H}_\Theta = \frac{\mathbf{C}^{-1}\mathbf{G}_\Theta}{\mathbf{G}_\Theta \cdot \mathbf{C}^{-1}\mathbf{G}_\Theta} \quad (3.10)$$

along with the global source power

$$S_\Theta^2 = \mathbf{H}_\Theta \cdot \mathbf{C}\mathbf{H}_\Theta = [\mathbf{G}_\Theta \cdot \mathbf{C}^{-1}\mathbf{G}_\Theta]^{-1} \quad (3.11)$$

The global neural activity index N_a [van Veen et al., 1997] is then calculated for every location and direction Θ and serves as a relative measure of activity originating from Θ . N_a comes in different flavors as distinguished by Huang et al. [Huang et al., 2004]. According to this classification, we shall be using the type III activity index (also used in synthetic aperture magnetometry), defined as

$$N_a = \frac{\mathbf{G}_\Theta \cdot \mathbf{C}^{-1} \mathbf{G}_\Theta}{\mathbf{G}_\Theta \cdot \mathbf{C}^{-1} \boldsymbol{\Sigma} \mathbf{C}^{-1} \mathbf{G}_\Theta}. \quad (3.12)$$

where $\boldsymbol{\Sigma}$ is the covariance matrix of the noise. $\boldsymbol{\Sigma}$ can be estimated from baseline data or chosen as a constant times the identity matrix. The denominator in (3.12) is a normalizing factor and serves the purpose of compensating for different magnitudes of the forward solutions that depend on the depth and the orientation of the sources as has been discussed in Chapter 2.5.

3.3 Invertibility of the Covariance Matrix

When certain conditions are met, the covariance matrix \mathbf{C} of the signals detected by the sensors is singular and its inverse does not exist. This happens in the case of low-dimensional signals, i.e. signals with a low noise level like averages, or in general, when the signal space has a dimension smaller than the number of sensors. There are two ways to deal with this problem: regularization and sub-space projection [Fuchs, 2007]. The method of subspace projection reduces the dimensionality to the subspace defined by the eigenvectors of the covariance matrix which correspond to eigenvalues that are significantly bigger than zero. In regularization (the method we used in our simulations), a constant ξ_r , representing uncorrelated noise, is added to the diagonal of the covariance matrix \mathbf{C} in order to create a non-singular matrix that is invertible and the beamformer activity index can be calculated. In our simulations the optimal value of the regularization parameter varied between 5×10^{-4} and 10^{-2} .

Anatomical Constraints and Realistic Head Geometry

4.1 Head Model: The Need for Realistic Geometry

The sources of the signals that are recorded by EEG on the scalp and MEG outside the head are mainly located in the cortical gray matter, where the pyramidal cells are organized in columns perpendicular to the cortical surface and activated coherently, producing tiny electric currents. Anatomically constrained beamforming takes advantage of this property and assumes that all current sources (modeled as electric dipoles) are located on this surface and produce currents perpendicular to it. Human cortex is a highly folded layer of neural tissue that covers the surface of the forebrain and its area across different subjects averages $0.12m^2$ per cortical hemisphere [Toro et al., 2008]. Though human brains have structural similarities across different subjects, variation in volume, shape of the head and complexity of the cortical folds make every brain unique. In addition, the shape of the skull is also unique. Therefore, to accurately estimate the neural activity in electroencephalography, both anatomical (such as the cortical surface and skull/skin interfaces) and electrophysiological data must be obtained from the same subject.

4.2 Extracting the Brain Surface: Freesurfer

The team from the Athinoula A. Martinos Center for Biomedical Imaging at Massachusetts General Hospital with support from CorTechs Labs, Inc., La Jolla, CA developed a powerful tool [Dale et al., 1999; Fischl et al., 1999] that allows one to extract the surface of the cerebral cortex from an MRI scan. This software package, called Freesurfer, is currently available for Mac OS and Linux platforms and utilizes complex and computationally intensive geometrical and topological filtering for surface extraction. It also takes into account that the cortical surfaces for each hemisphere are singly connected and topologically equivalent to a sphere¹ [Fuchs, 2002]. The output from Freesurfer is shown in Figure 4.1 and contains two closed surfaces of the gray-white matter boundary, consisting of approximately 284,000 vertices and 568,000 triangles. This high-resolution tessellation allows one to achieve a localization accuracy of the dipolar current sources of about 1mm.

4.3 Extracting Skull and Scalp Surfaces

The EEG forward model [Mosher et al., 1999] used here is based on a multi-shell head model that takes three different surfaces into account: cortex, skull (inside and outside) and scalp. There are three layers of different conductivity separated by these surfaces: cerebrospinal fluid, skull (bone) and skin. The smearing of the EEG signal from the cortex happens primarily near the interface between the skull and the scalp [Nunez, Srinivasan, 2006]. The potential is greatly attenuated when passing through the skull and therefore the thickness of the skull in different regions of the head is important. One way of obtaining these head surfaces is to use a computed tomography (CT) scan. The CT scan shows the bone bright and easily recognizable

¹This is possible if the corpus callosum connecting left and right hemispheres is cut.

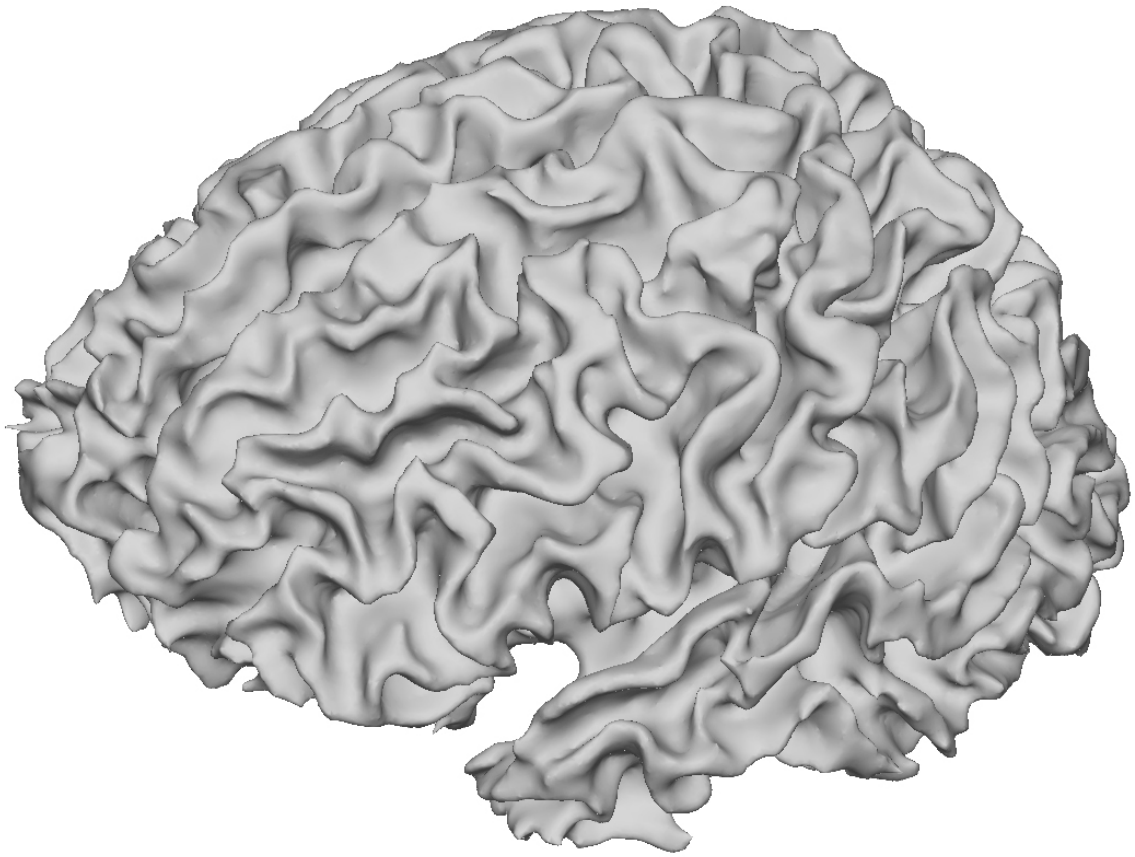


Figure 4.1: Gray-white matter boundary surface extracted from an MRI scan using Freesurfer. The tessellation consists of approximately 284,000 vertices and 568,000 triangles.

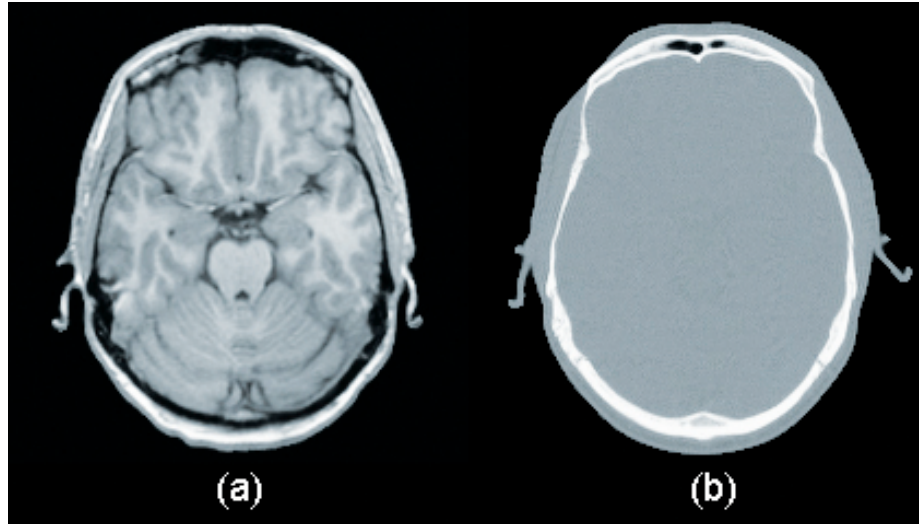


Figure 4.2: MRI scan versus CT scan. On the MRI scan (a) bone is difficult to identify, whereas on the CT scan (b) bone is bright and easily recognizable.

(Fig. 4.2b) compared to an MRI scan (Fig. 4.2a) where bone appears dark due to its low water content and is much more difficult to identify. The bone and skin surfaces are extracted from a CT scan and used in the boundary element method (BEM) for the EEG forward solution. The skin surface also serves as a constraint for the EEG electrode locations.

The resulting surface tessellations (648 vertices each) of the CSF (blue), skull (yellow) and skin (red) are shown in Figure 4.3. The bottom of each surface is constructed such that the BEM requirement of closed surfaces is satisfied and at the same time fully encloses the gray matter inside the CSF volume. This construction can be justified by the fact that we are interested only in values of the electric potential at EEG electrode locations (shown as green dots overlaying the scalp surface).

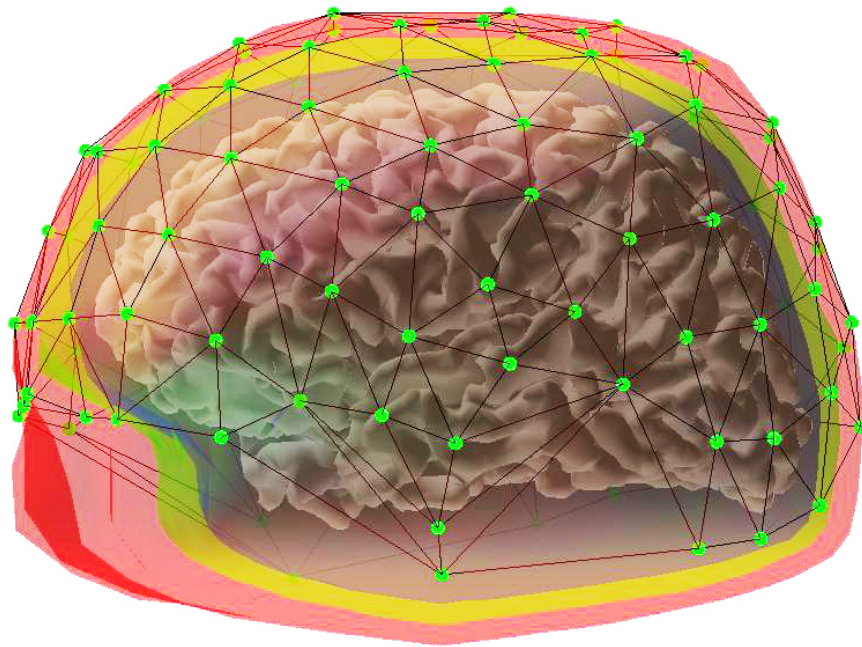


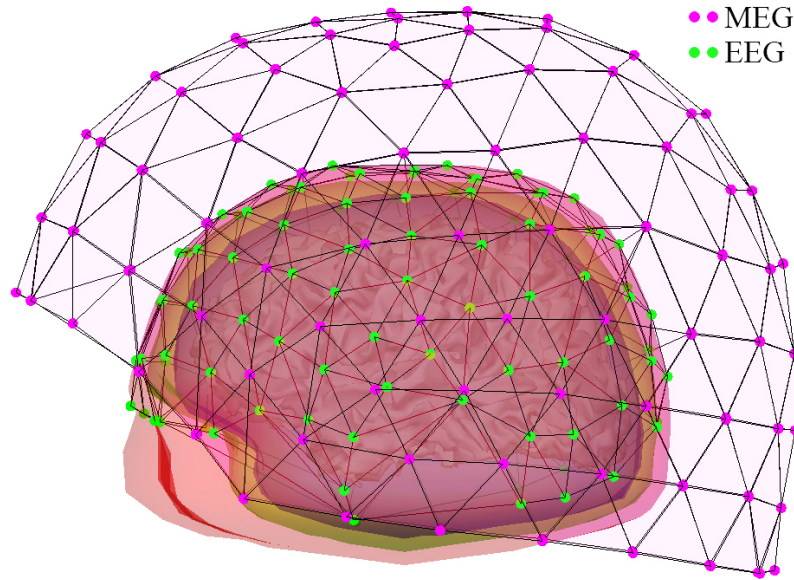
Figure 4.3: Head surfaces extracted from a CT-scan (red: scalp, yellow: skull, blue: cerebrospinal fluid) and from an MRI scan (gray: gray-white matter boundary). EEG electrodes are taken from a 122 channel montage and are shown as green dots overlaying the scalp surface.

Beamforming Simulations

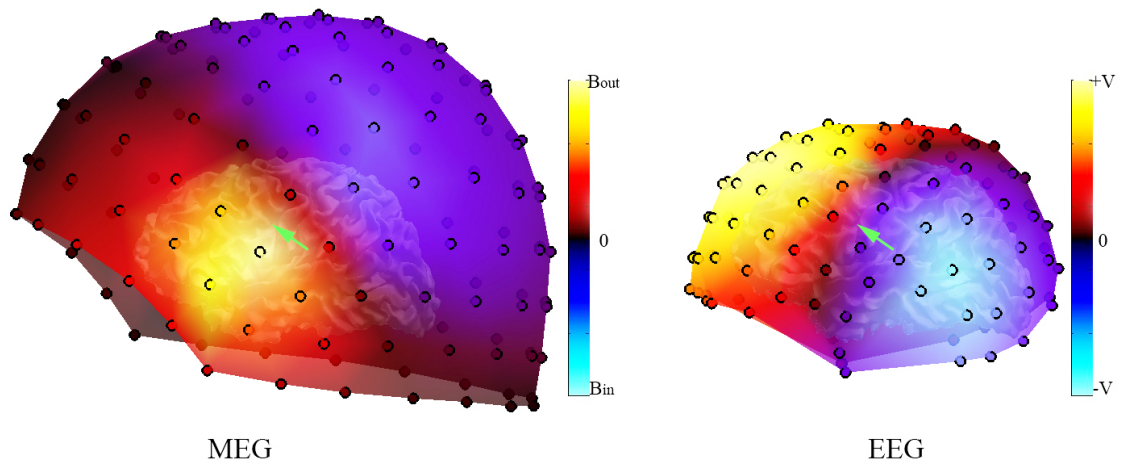
5.1 EEG and MEG Data Sets

In previous chapters we established the mechanism for EEG/MEG source localization using anatomically constrained beamforming which we will test on a simulated EEG data set. This data set is created by activating a certain electric dipole (or a set of them) with a time course, for instance, a damped oscillator function. In order to make the simulated data more realistic, two types of noise are induced onto the source and its environment (the rest of the brain). For the former, white noise is added to the dipole moment amplitude, whereas the latter is implemented by activating a randomly chosen set of 100 dipoles at each time step. The data set is obtained by using the principle of superposition of the electric fields which allows merging of the forward solutions from the source dipoles with the forward solutions of randomly activated currents.

Figure 5.1(a) shows the relative positions of the MEG coils and EEG electrodes with respect to the head. EEG electrodes are placed directly on the scalp surface while MEG coils are several centimeters away from the head. This is caused by the thermal shielding that separates the head from the liquid helium cooled MEG coils (SQUIDS). Figure 5.1(b) shows an example of the MEG and EEG forward solutions calculated from a single dipole source (green arrow). The strength and the direction

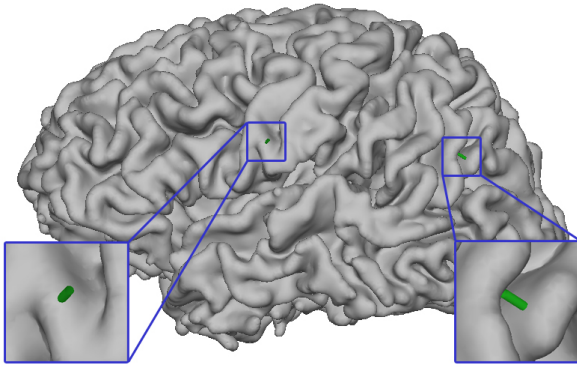


(a) 148 MEG coils and 122 EEG electrodes.

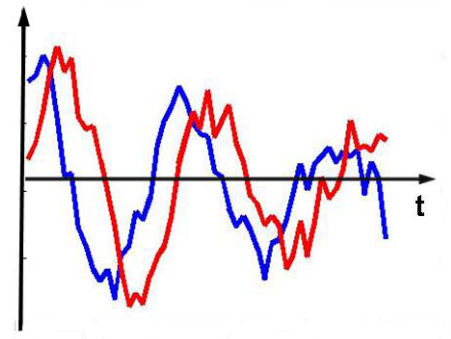


(b) MEG and EEG forward solutions (from a single dipole source, located in the left hemisphere with the direction as shown) are almost orthogonal to each other.

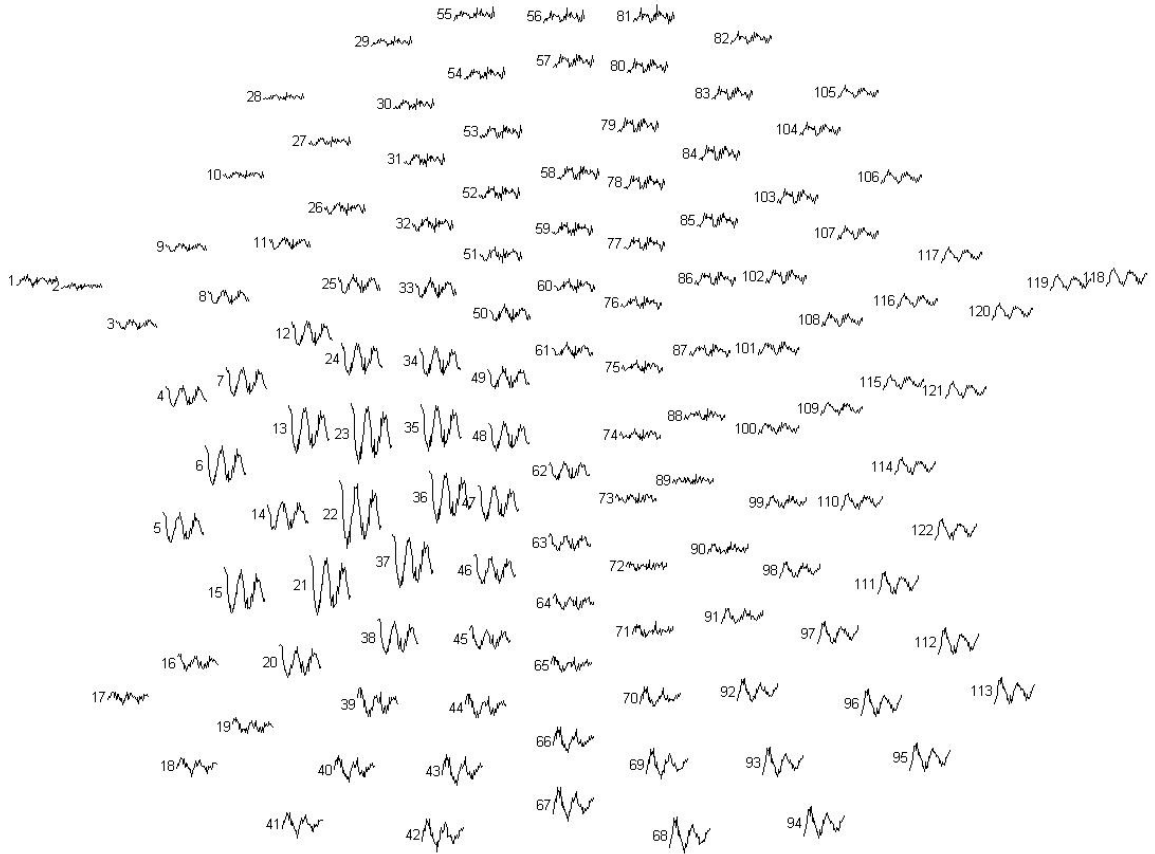
Figure 5.1: EEG and MEG sensor locations and examples of forward solutions.



(a) The sources: two dipolar currents in the left hemisphere.



(b) Time series of the two source dipoles: damped oscillators with noise and a phase shift of $\pi/2$ rad.



(c) Simulated EEG data of a montage, consisting of 122 electrodes.

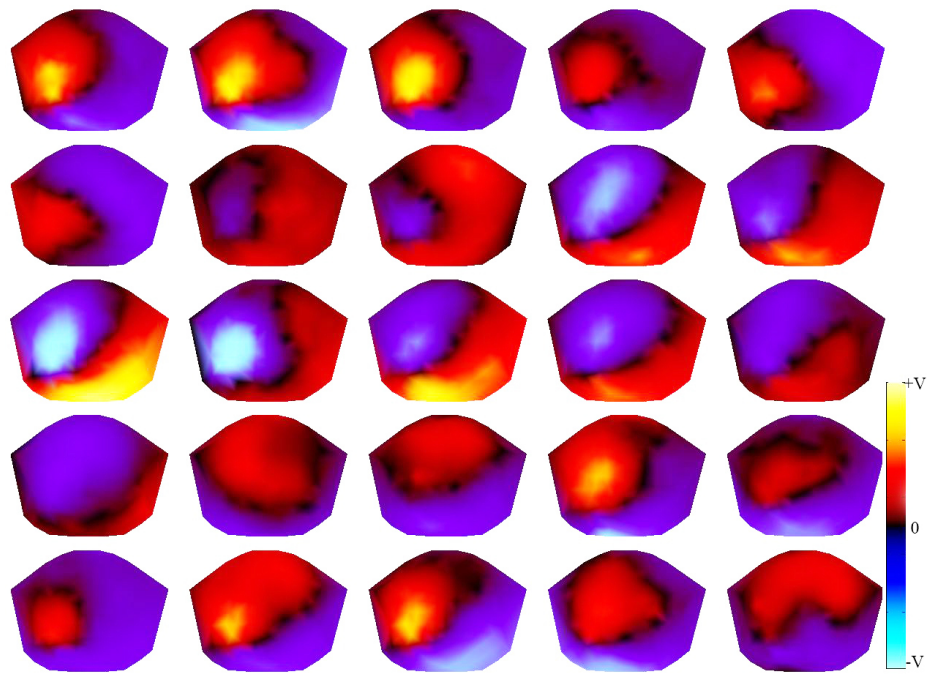
Figure 5.2: A simulated EEG data set using two dipoles as main sources of neural activity.

(pointing inside or outside the surface) of each dipole can be modeled by scaling the forward solution, i.e. all values at the sensors for a given solution are multiplied by a constant between -1 and 1.

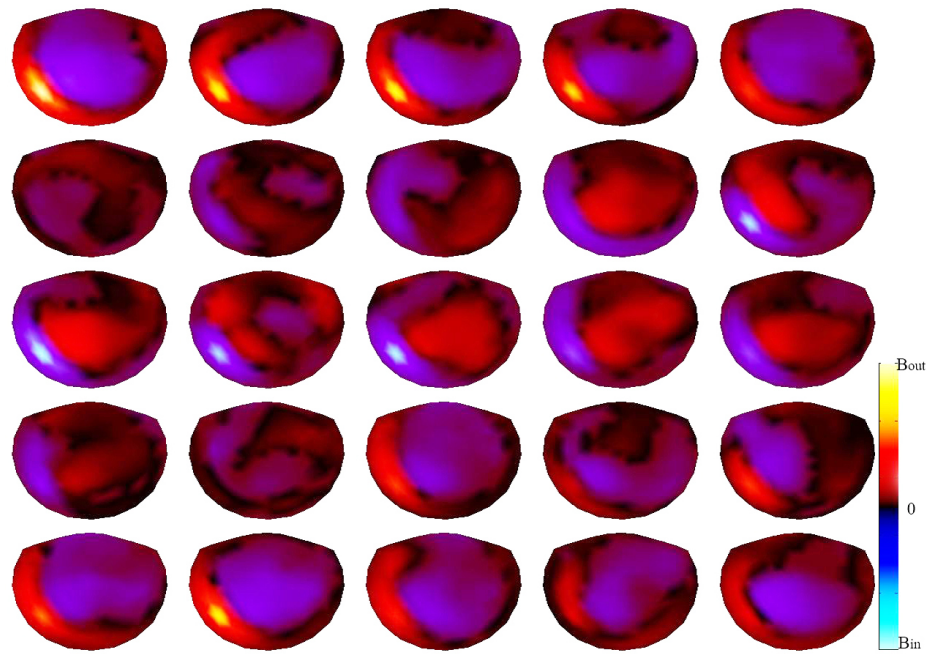
Figure 5.2(c) shows an example of a simulated EEG data set. Here the sources are two dipole currents in the left hemisphere as shown in Figure 5.2(a). The time series, consisting of 50 time-points for each of the source dipoles, shown in Figure 5.2(b), are damped oscillators with a phase shift of $\pi/2$ rad and additive noise. The forward solutions for these two dipoles plus 100 randomly chosen locations on the cortex are superimposed at each time step. The resulting simulated EEG and MEG data sets are shown in the form of topo plots in Figure 5.3. The time runs from left to right, top to bottom. Yellow corresponds to positive and blue to negative potential on the scalp surface for EEG. The outward radial component of the magnetic field through the MEG coils is shown in yellow; inward pointing magnetic field lines are shown in blue.

5.2 Realistic versus Spherical Head Models

For a comparison of the different head models we calculated EEG forward solutions for all three methods described in Chapter 2: single sphere, multi-shell and boundary element method. Figure 5.4 shows examples of forward solutions for a single dipole source in the left hemisphere for the different models. The single sphere model, which does not take the conductivity of the skull into account, provides a more localized distribution of the electric potential and due to its unrealistic assumptions is the least accurate. The next two graphs to the right in Figure 5.4 represent forward solutions calculated for the same multi-shell geometry but using two different methods: infinite sum and boundary elements. As can be seen and also verified by quantitative com-



(a) EEG



(b) MEG

Figure 5.3: Electric potential and corresponding magnetic field patterns: single dipole source in the left hemisphere (interpolated between 122 EEG sensors and 148 MEG coils) at 25 time points (left to right, top to bottom).

parison, these two methods provide identical results. The boundary element method applied to the realistic geometry not only gives a more accurate EEG forward solution, but also changes the accuracy of the beamforming source reconstruction significantly, when compared to spherical models. This can be demonstrated by using the spherical forward solutions to calculate the beamformer weights from a data set created with the realistic geometry model. When using spherical models, the regions that are expected to be more or less accurate are the frontal and occipital lobes as they are at similar distances to the skull surface in both spherical and realistic geometries. On the other hand, since the brain is not spherical, the temporal lobes are expected to be the source of the largest error. Figure 5.5(a) shows the activity estimated using spherical beamforming on a realistic EEG signal and the source appears to be widespread. For comparison, realistic geometry beamforming, as shown in Figure 5.5(b), provides a much more accurate estimate.

5.3 Single Dipole Source Current

In the first step we apply the beamforming method to a single dipole source EEG, patterns of which are shown in Figure 5.6. Calculation of the beamformer activity index N_a and reconstructed time series $X_{\Theta}^{rec}(t)$ starts with the covariance matrix \mathbf{C} , the components of which are

$$C_{ij} = \frac{1}{T} \int_0^T X_i(t)X_j(t)dt \quad (5.1)$$

where $X_i(t)$ is the time series on the i^{th} EEG sensor. In order to calculate the beamformer weights \mathbf{H}_{Θ} we need the inverse of the covariance matrix \mathbf{C}^{-1} and the forward solutions \mathbf{G}_{Θ} from all locations Θ on the cortical surface. The latter is pre-calculated for different head models and the former requires a regularization parameter to be added to the diagonal in order to be invertible. The beamformer weights are then

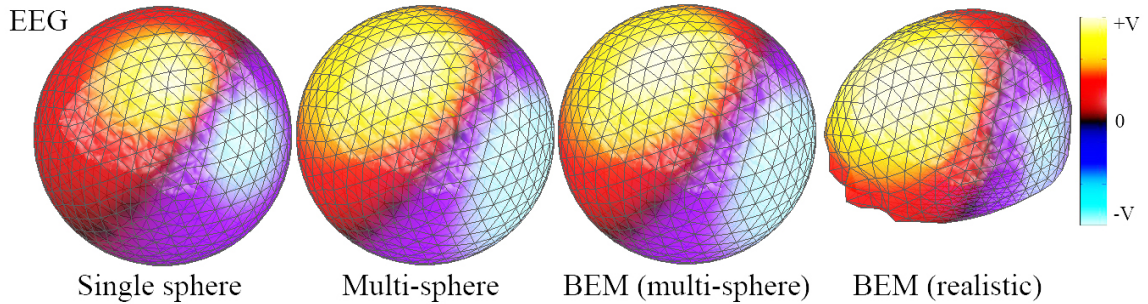
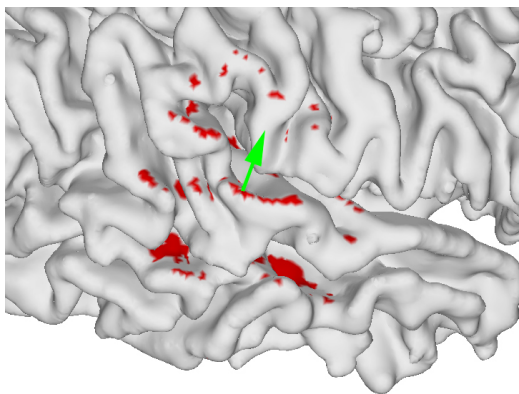
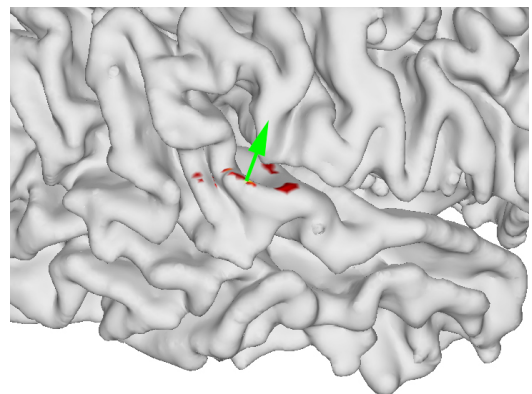


Figure 5.4: EEG forward solutions comparison for different head models with a dipolar current source in the left hemisphere. Forward solutions are calculated using a single sphere model, multi-sphere model, and the boundary element method applied to both multi-sphere and realistic geometry.



(a) Activity detected applying the multi-sphere forward solution.



(b) Activity detected applying the realistic geometry forward solution.

Figure 5.5: Comparison of the electric activity (red) detected from a single source (green arrow) when spherical and realistic geometry forward solutions are used. Realistic geometry model offers a more accurate source reconstruction.

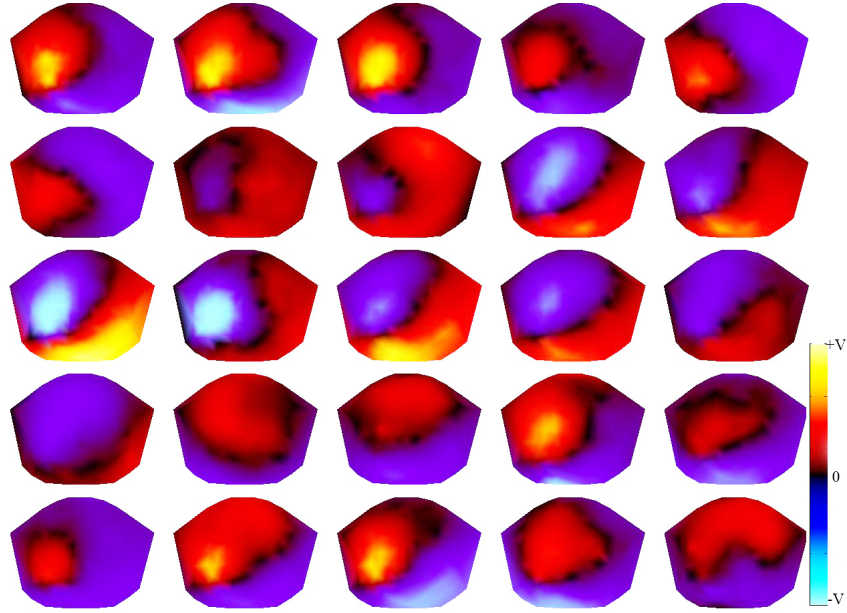


Figure 5.6: Simulated EEG patterns: single dipole source, located in the left hemisphere as shown in Figure 5.7.

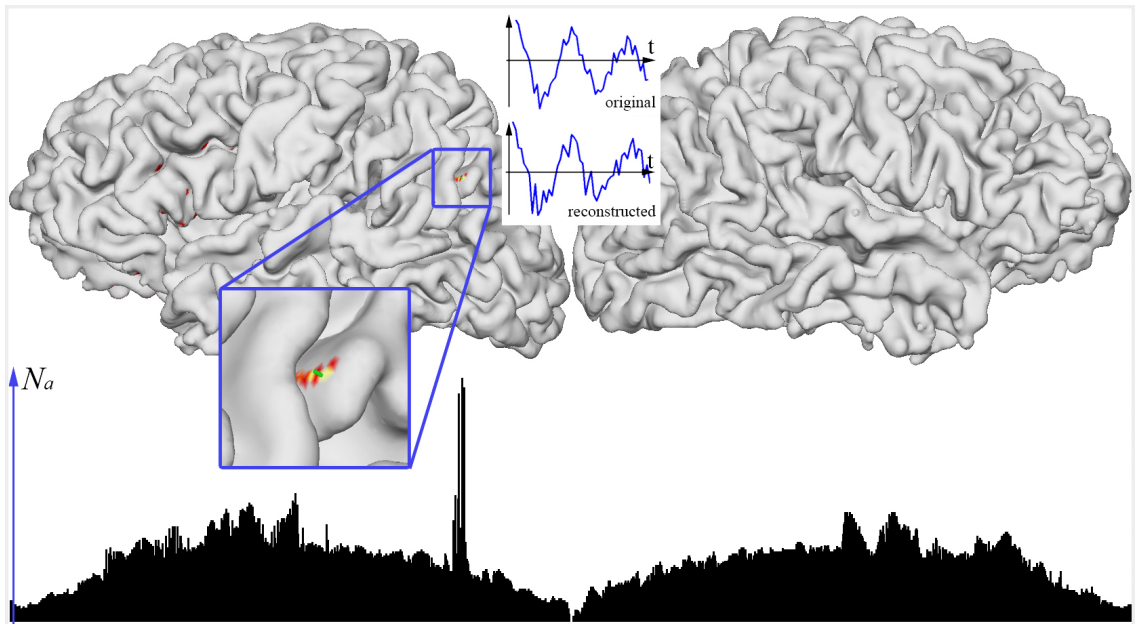


Figure 5.7: Beamforming activity index: single dipole source. The time course of the source current (at the location in the left hemisphere as shown) is a damped oscillator with noise. The beamformer activity index N_a is plotted on the cortical surface (top) and as a function of the vertex coordinate in the longitudinal direction (bottom). The threshold for the values of N_a when plotted on the cortical surface is the average of N_a plus three standard deviations ($\bar{N}_a + 3\sigma$).

obtained from

$$\mathbf{H}_\Theta = \frac{\mathbf{C}^{-1}\mathbf{G}_\Theta}{\mathbf{G}_\Theta \cdot \mathbf{C}^{-1}\mathbf{G}_\Theta} \quad (5.2)$$

and the beamforming activity index N_a is calculated as

$$N_a = \frac{\mathbf{G}_\Theta \cdot \mathbf{C}^{-1}\mathbf{G}_\Theta}{\mathbf{G}_\Theta \cdot \mathbf{C}^{-1}\Sigma\mathbf{C}^{-1}\mathbf{G}_\Theta} \quad (5.3)$$

The reconstructed time series reads

$$X_\Theta^{rec}(t) = \mathbf{X}(t) \cdot \mathbf{H}_\Theta \quad (5.4)$$

where \mathbf{H}_Θ are the beamformer weights calculated for the location and direction Θ and $\mathbf{X}(t)$ is the EEG signal at the electrodes.

An example of a beamformer reconstruction of neural activity is shown in Figure 5.7¹. We consider a source dipole Θ , placed in the left hemisphere on the white matter surface with a direction perpendicular to that surface. The source is given a time series $X_\Theta^{orig}(t)$ (middle) – a damped oscillator with noise. The hemispheres are arranged in a continuous fashion (from left to right: left hemisphere is anterior-to-posterior, right hemisphere is posterior-to-anterior) such that the bottom graph, representing the beamformer activity index N_a in arbitrary units, is plotted as a function of the longitudinal coordinate of the vertices on the cortical surface of a given hemisphere. The threshold for the values of N_a when plotted on the cortical surface is the average of N_a plus three standard deviations ($\bar{N}_a + 3\sigma$).

Visual inspection of the graph of the beamformer activity index in Figure 5.7 (bottom) allows to determine the number and approximate location of regions with a signal strength significantly larger than the mean activity of the rest of the brain. It also gives an estimate of the signal-to-noise ratio and how the detected activity is spread out in the space surrounding the source. The beamformer activity index

¹This layout will be used to present most of the simulation results and will be given a thorough explanation in this section.

values are plotted color-coded (with a threshold to remove the noise) on the cortical surface (top), and blow-ups are provided for better visualization of the detected local activity around the dipole.

The beamformer activity index in Figure 5.7 has a single sharp spike, which corresponds to the location of the dipole source in the left hemisphere and a series of smaller spikes, corresponding to sources with location and direction close to the original dipole and therefore with a similar forward solution. The reconstructed time series is plotted below the original and reproduces the damped oscillatory function and its frequency.

5.4 Two Dipole Source Currents

In this analysis we first look at two distant source dipoles: one in each hemisphere as shown in Figure 5.9. Simulated EEG patterns for these dipoles (the time courses are damped oscillators with a phase shift and noise) and randomly active sources are shown in Figure 5.8. The calculated beamformer activity index now shows two regions of activity, corresponding to the source locations and surrounding areas. The time series for the dipole sources are also reconstructed and reproduce the original damped oscillations.

If two dipoles are close to each other as shown in Figure 5.11, it is very difficult, if not impossible, to distinguish these sources from a visual analysis of the EEG patterns, which are shown in Figure 5.10. However, the beamformer activity index in this case detects two areas of activity, even though the sources are only about 1cm apart. In addition, the damped oscillatory time series at the source locations are reconstructed.

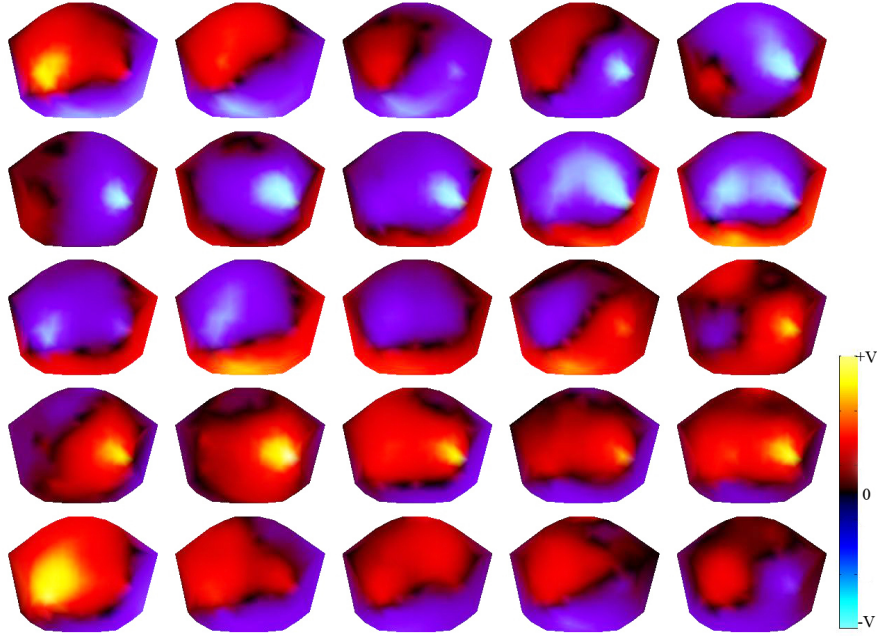


Figure 5.8: Simulated EEG patterns: two spatially distant dipole sources located in left and right hemispheres as shown in Figure 5.9.

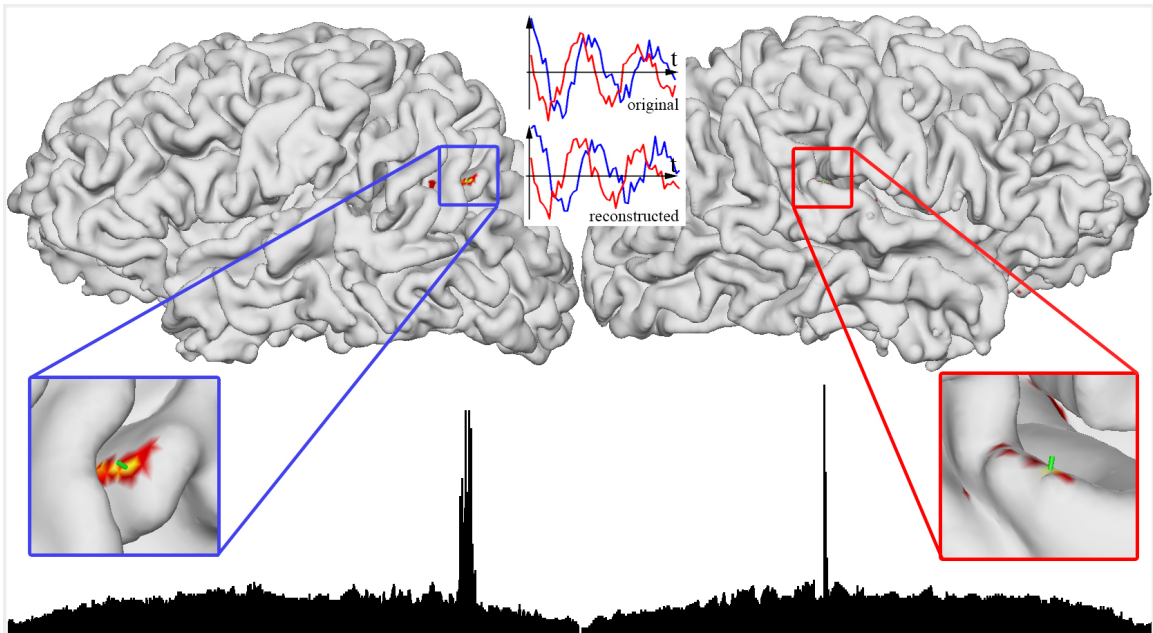


Figure 5.9: Beamforming activity index: two spatially distant dipole sources located in the left and right hemisphere as shown. The beamformer activity index is plotted on the cortical surface (top) and as a function of the vertex coordinate in the longitudinal direction (bottom). The threshold for the values of N_a when plotted on the cortical surface is the average of N_a plus three standard deviations ($\bar{N}_a + 3\sigma$).

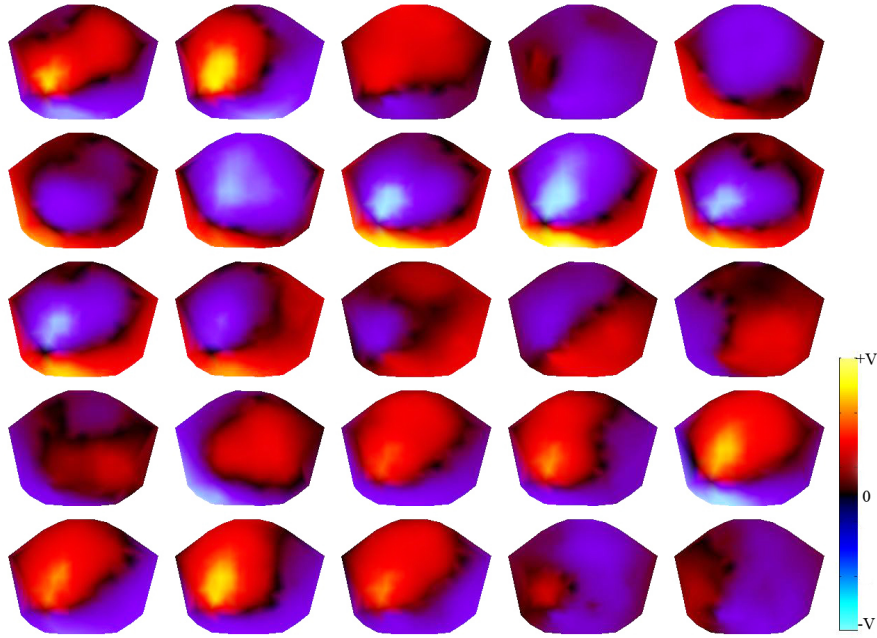


Figure 5.10: Simulated EEG patterns: two spatially close dipole sources located in the left hemisphere as shown in Figure 5.11.

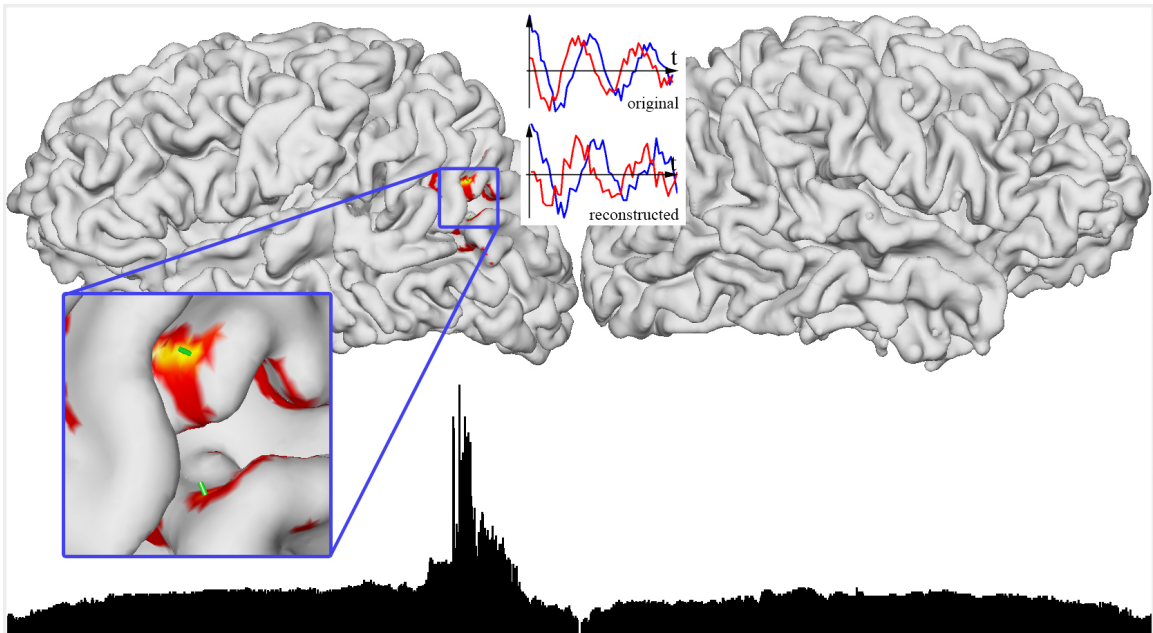


Figure 5.11: Beamforming activity index: two spatially close dipole sources located in the left hemisphere as shown. The beamformer activity index is plotted on the cortical surface (top) and as a function of the vertex coordinate in the longitudinal direction (bottom). The threshold for the values of N_a when plotted on the cortical surface is the average of N_a plus three standard deviations ($\bar{N}_a + 3\sigma$).

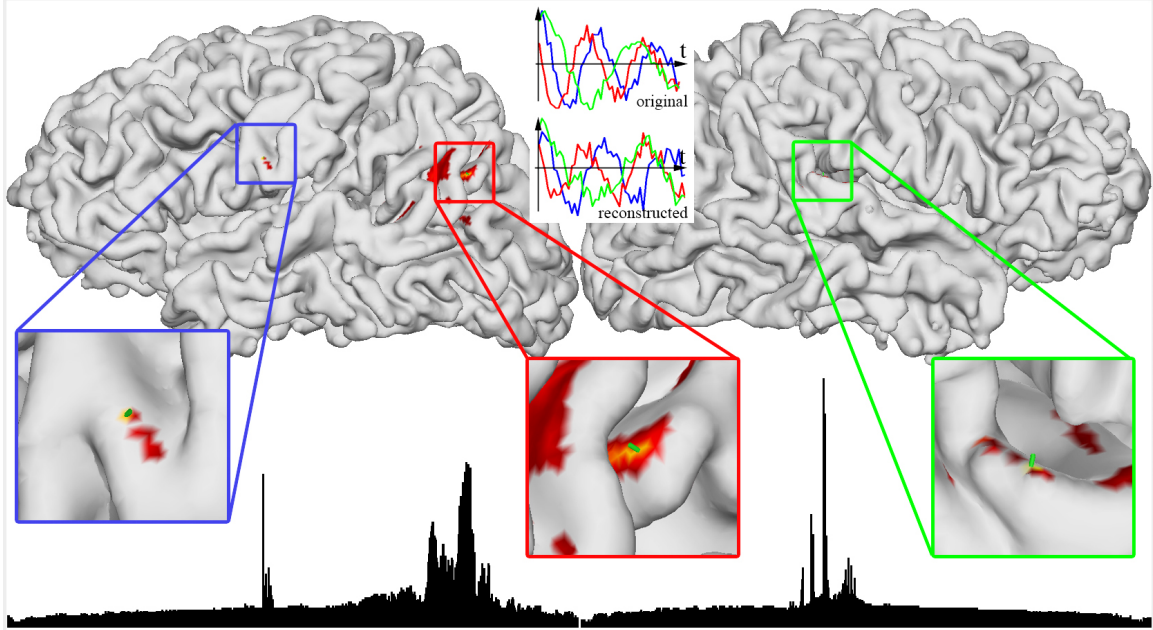


Figure 5.12: Beamforming activity index: three dipole sources. The time courses feature phase and frequency shifts. The beamformer activity index is plotted on the cortical surface (top) and as a function of the vertex coordinate in the longitudinal direction (bottom). The threshold for the values of N_a when plotted on the cortical surface is the average of N_a plus three standard deviations ($\bar{N}_a + 3\sigma$).

5.5 Three-Source Beamforming Simulation

So far we have established that the beamforming method works correctly for a single source current or two uncorrelated sources, the time courses of which are shifted by a quarter of a cycle. In our next simulation we add a third source.

Since beamforming is based on the calculation of the covariance matrix of the signal from the EEG electrodes, the activity index will likely fail to distinguish between the source locations, if any of the sources are strongly correlated. This is especially the case for dipoles for which the forward solutions are similar, like spatially close and/or parallel sources. For three dipoles, it is not sufficient to introduce another shift of the oscillatory time series in the time domain, because in that case one of

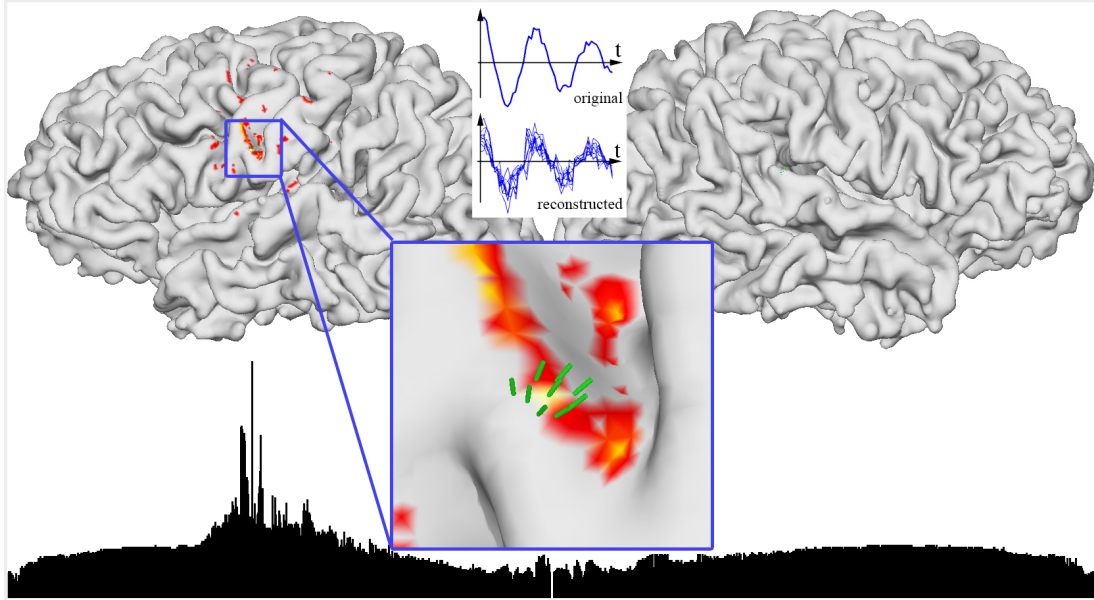


Figure 5.13: Beamforming activity index: a single patch of nine dipoles with the same time series of damped oscillator with noise. The threshold for the values of N_a when plotted on the cortical surface is the average of N_a plus three standard deviations ($\bar{N}_a + 3\sigma$).

the damped sinusoidal functions can always be represented as a linear combination of the other two and the beamforming activity index will only be able to detect two locations out of three. Therefore, in order to create uncorrelated sources, we use a different frequency. An example with three dipoles is shown in Figure 5.12. The beamforming activity index shows three regions of activity, and the time series are reconstructed accurately. This method was also tested with four and five dipoles and yielded satisfactory results.

5.6 Extended Sources

Neural activity can be modeled as source dipoles, as was shown in the previous sections. As a next step, a certain region on the cortical surface, described by a number of dipoles, is activated with the same time course for all sources within the patch.

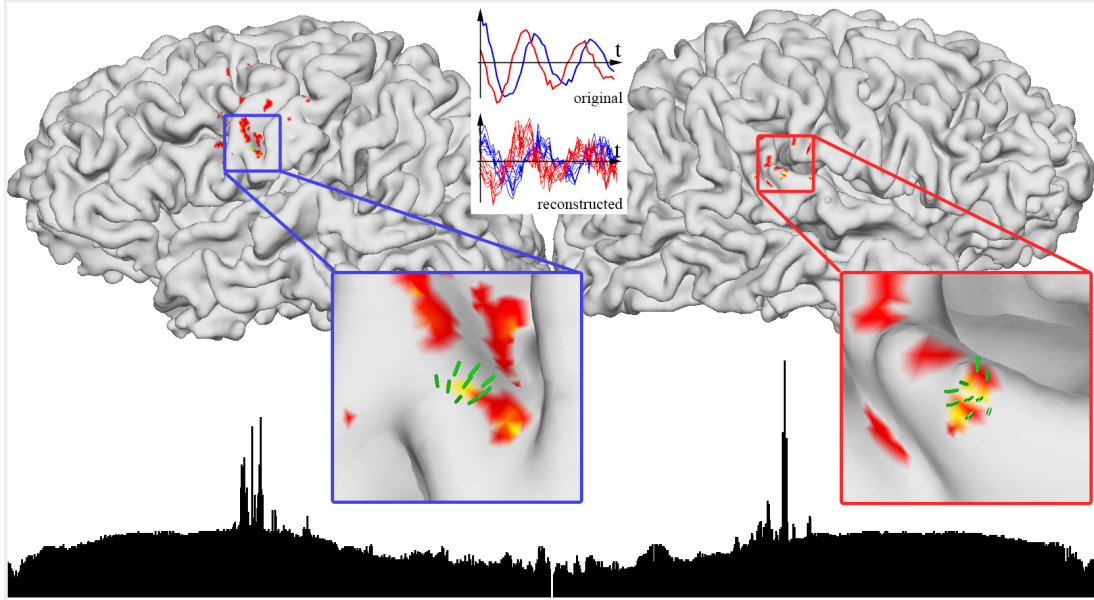


Figure 5.14: Beamforming activity index: two patches of nine source dipoles. The time course of all dipoles within a patch is a damped oscillator with noise. Time courses between the patches are different by a phase shift of $\pi/2$ rad. The threshold for the values of N_a when plotted on the cortical surface is the average of N_a plus three standard deviations ($\bar{N}_a + 3\sigma$).

First simulation is performed for a dipole in the left hemisphere and all of its nearest neighbors. A total of nine dipoles have the same time course labeled 'original' in Figure 5.13. The beamforming activity index allows to accurately locate the detected sources on the cortical surface and the highest value of activity corresponds to the center of the patch. This means that the input of the sources surrounding the center dipole is amplifying the signal from the center of the patch. The reconstructed time series of each of the nine dipole sources is also shown in Figure 5.13: the damped oscillatory behavior is reconstructed on all nine sources.

The second example of extended sources of activity consists of two patches of dipoles. In addition to the patch source in the left hemisphere found previously, another area of nine dipoles is activated in the right hemisphere. The original and

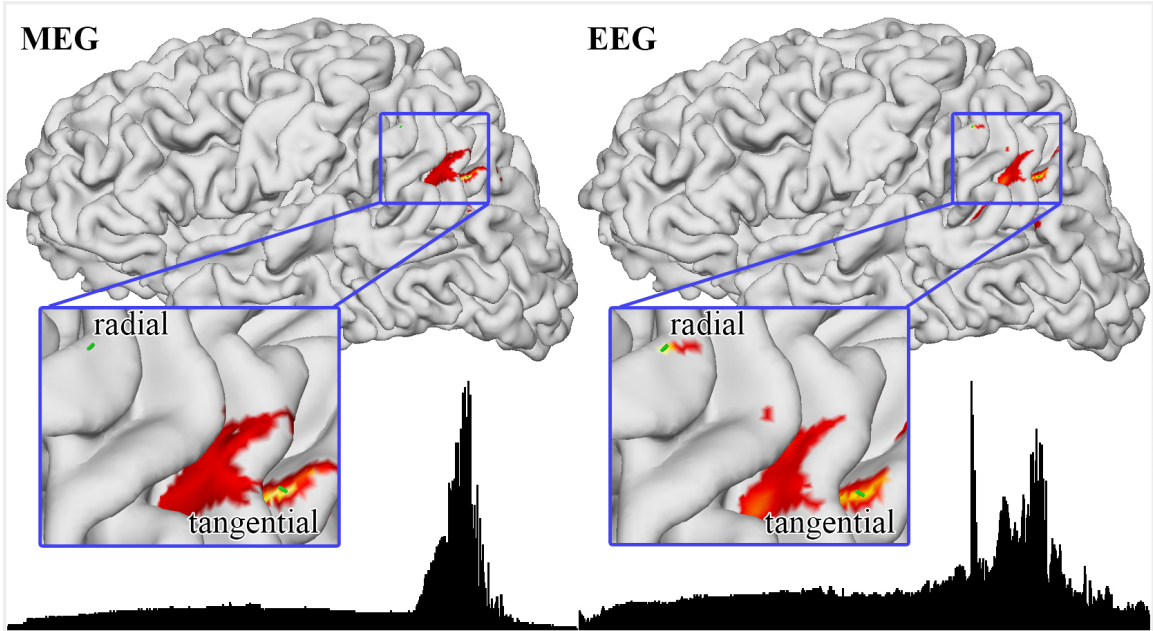


Figure 5.15: Beamforming activity index: MEG beamforming versus EEG beamforming. MEG is insensitive to the radial source. The beamformer activity index is plotted on the cortical surface and as a function of the vertex coordinate in the longitudinal direction (bottom). The threshold for the values of N_a when plotted on the cortical surface is the average of N_a plus three standard deviations ($\bar{N}_a + 3\sigma$).

reconstructed time series, and the beamforming activity index are shown in Figure 5.14. Both locations are accurately detected on the cortical surface and their time courses are satisfactorily reconstructed.

5.7 EEG versus MEG: Radial Sources

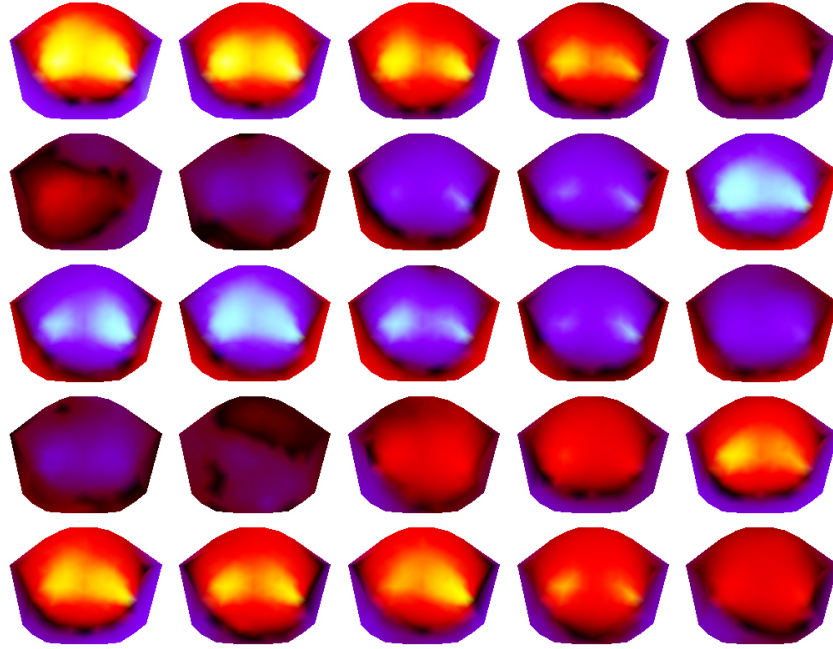
As discussed in Chapter 2.2, MEG is insensitive to radial currents. Here we investigate how source reconstruction is affected by the direction of the source. To this end we compare EEG versus MEG beamforming applied to both radial and tangential sources. In this simulation the source currents are located in the left hemisphere and the time series on the dipoles are damped oscillators with noise and time shift. The

results are shown in Figure 5.15, from which it is evident that EEG beamforming analysis detects strong activity coming from both source locations. In contrast, MEG beamforming is only capable of detecting the tangential source. This means that EEG beamforming may become a valuable addition to the MEG and fMRI source localization methods.

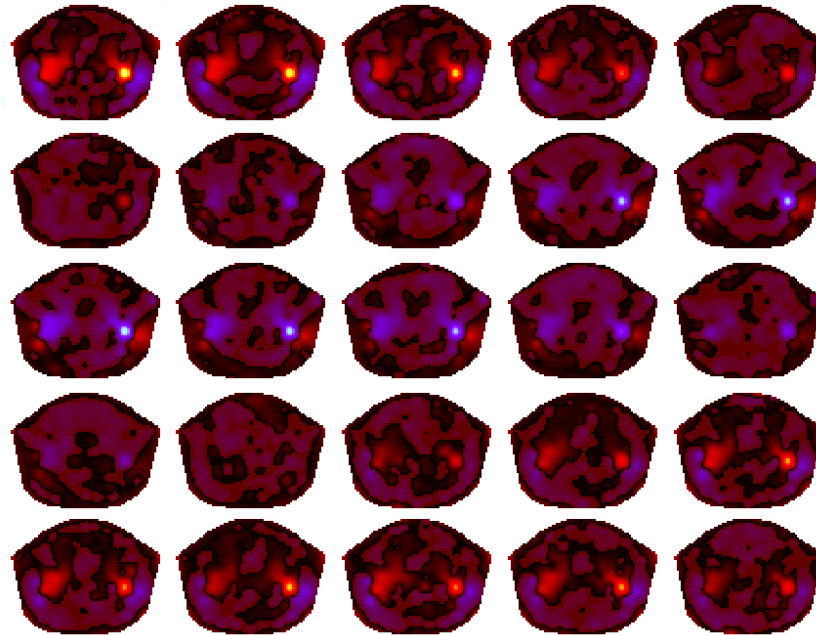
Another important conclusion can be made from the plot of the EEG beamforming activity index: the radial source is localized with higher accuracy compared to the tangential source. This is caused by a fact mentioned earlier in Chapter 2 and shown in Figure 5.1: EEG is most sensitive to currents located on top of gyri, the sources closest to the surface of the skull, the directions of which are mostly radial. They create higher values of the electric potential on the scalp surface, and therefore have a higher magnitude of the forward solution, which leads to a better signal-to-noise ratio. In addition, the electric potential created by tangential currents is taking a path almost parallel to the skull, which causes higher values of angular deflection and the potential on the scalp is more smeared out and attenuated. All this makes radial currents more favorable for EEG beamforming and activity index more focused.

5.8 Correlated Sources: Surface Laplacian

All of the previous EEG beamforming simulations work well with uncorrelated sources, i.e., the time series of any one of the sources cannot be represented as a linear superposition of the rest of them. In real situations, however, there are regions in the brain that are activated simultaneously, for instance, when a subject is exposed to binaural stimuli. Both, left and right primary auditory cortices are active at the same time, and these two areas as sources are spatially distant but temporally correlated. Simulated EEG patterns, which correspond to the described setup are shown in Figure



(a) EEG pattern for a binaural stimulus at 25 time points (left to right, top to bottom).



(b) Surface Laplacian calculated from the patterns in (a).

Figure 5.16: Simulated EEG data set and corresponding surface Laplacian: binaural stimulus. The sources are located in the left and right auditory cortices.

5.16(a). The electric potential distributions, due to the source dipoles being mostly parallel to each other, overlap and reinforce each other. If we apply the beamforming algorithm to this EEG data set, the calculated activity index shows a broad area located mostly at the center of the brain as shown in Figure 5.17.

Figure 5.16(b) shows the surface Laplacian calculated from the simulated EEG data set. As described in detail in Chapter 2.4, the surface Laplacian allows one to estimate the cortical potential, which is much more localized than the scalp potential because it is not blurred by the skull-skin interface. The two areas of activity are now visually distinguishable. The surface Laplacian of each of the forward solutions corresponding to a unique location and direction on the cortical surface is calculated in order to apply the beamforming algorithm. The beamformer weights are obtained the same way as before, but with the values of the surface Laplacian used instead of electric potential as the time series $\mathbf{X}(t)$. The results are shown in Figure 5.18. Two areas of strong activity, one in each hemisphere, are now detected, and when plotted on the cortical surface, reveal locations in the primary auditory cortices. The reconstructed time series, however, are extremely noisy and do not match the original activation as shown in Figure 5.18 (top center).

Since the neural activity in the auditory cortices is highly correlated, the beamforming analysis (based on covariance) fails to return the oscillatory behavior of the sources (Figure 5.18). To solve this problem, we apply the beamforming procedure and calculate the activity index on the cortical surface using only a subset of EEG electrodes located on the left or on the right side of the head, which allows to eliminate interference from the electrodes on the opposite side. This procedure is applied to both hemispheres and the results are shown in Figure 5.19. The time series corresponding to the sources in the left and right hemisphere are shown in blue and red, respectively. The middle and bottom graphs on the right in Figure 5.19 show

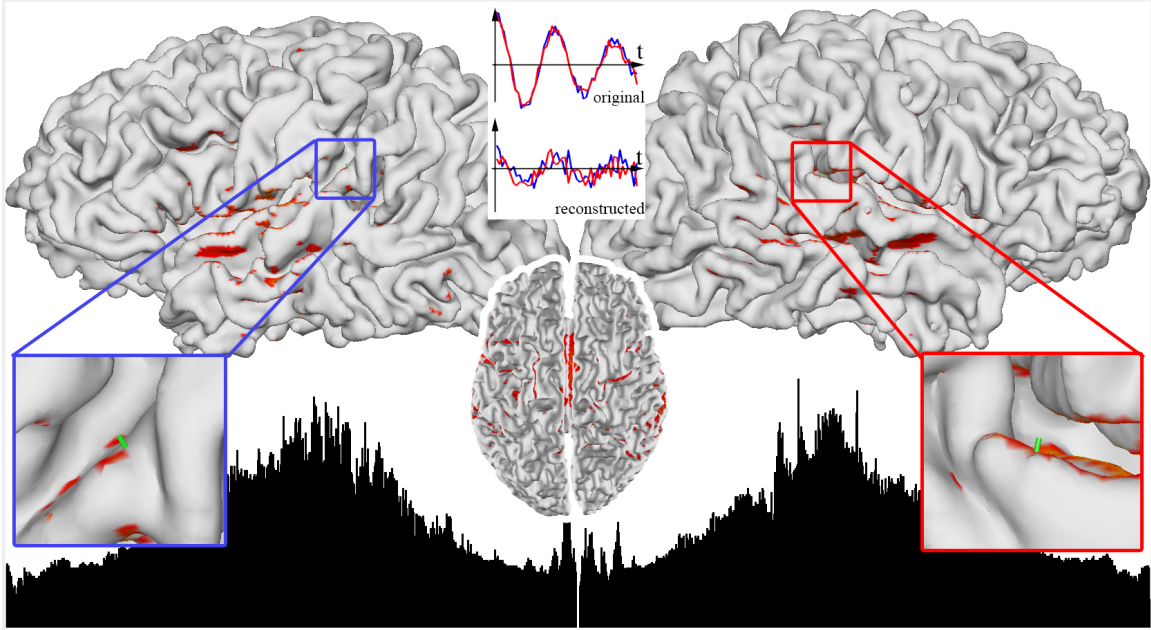


Figure 5.17: Beamforming activity index calculated from the EEG forward solution. Two highly correlated sources are located in the primary auditory cortices.

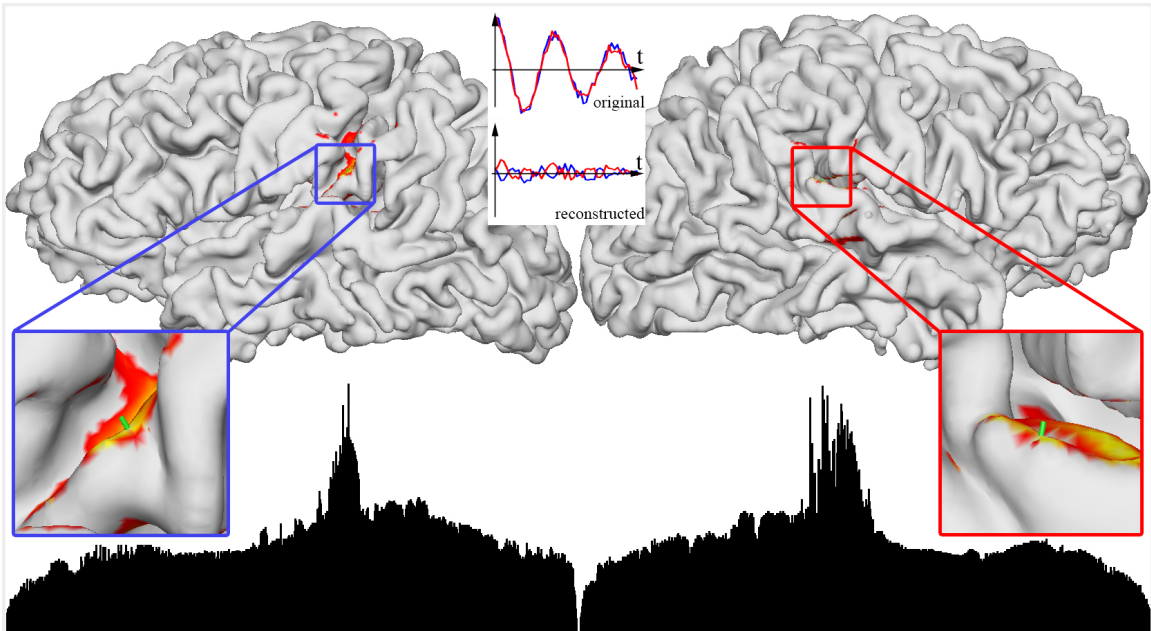


Figure 5.18: Beamforming activity index calculated using the surface Laplacian derived from the EEG forward solution. Two highly correlated sources are located in the primary auditory cortices.

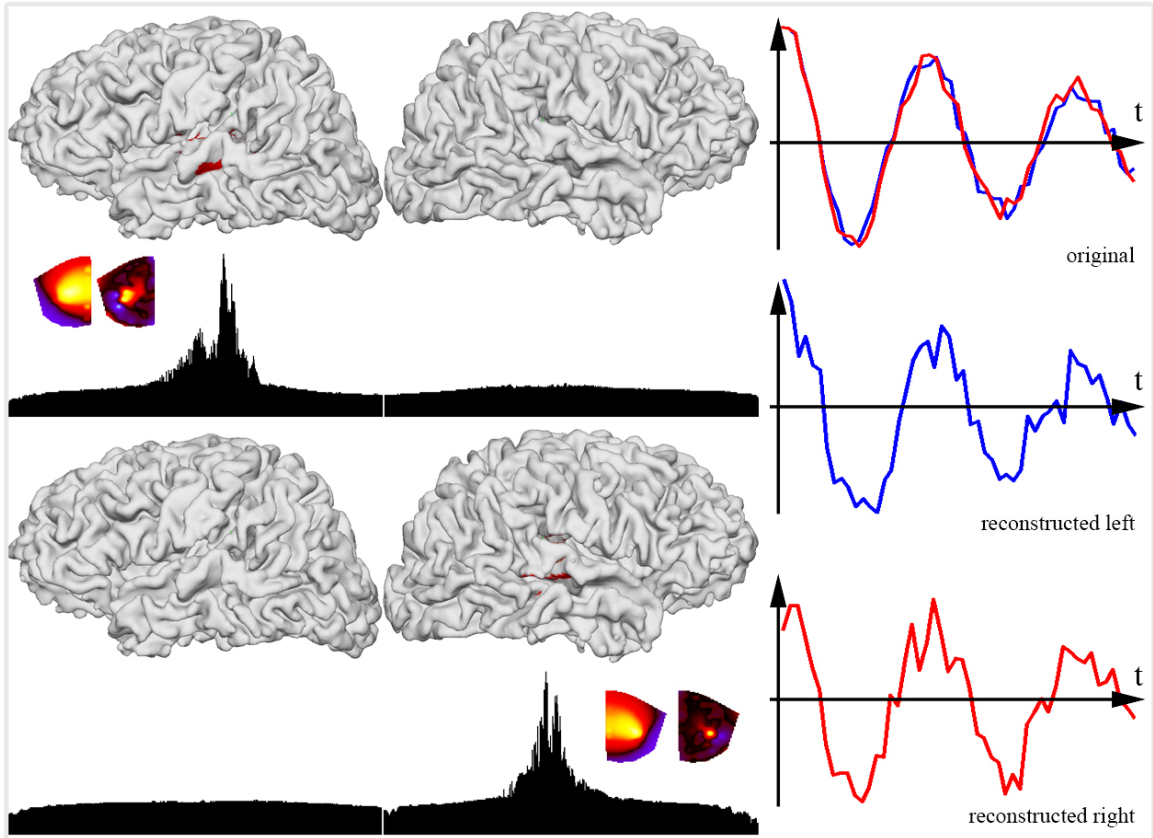


Figure 5.19: Beamforming activity index and reconstructed time courses calculated using surface Laplacian from two subsets of EEG sensors: left and right hemisphere.

how the time courses are reconstructed when only half of the sensors are used in the beamforming analysis: left source activity (blue) is accurately reproduced as shown in the middle and the red curve in the bottom graph corresponds to the dipole in the right hemisphere.

5.9 Summary of the EEG Beamforming Simulations

In the present study we have developed a procedure that allows for neural source reconstruction from EEG data. In the first part, anatomically constrained minimum

variance beamforming is applied to a realistic geometry head model that takes into account the shape of the head, thickness and conductivity of the head layers: CSF, skull and scalp. The current sources, modeled as dipoles, are constrained to the surface of the white matter. The realistic geometry model is compared to spherical models and it is demonstrated in Figure 5.5 that implementing a realistic instead of a spherical forward solution increases the spatial resolution and accuracy of the current source reconstruction. The EEG data is simulated at every point in time by superimposing the forward solutions from the main sources (dipoles with a damped oscillatory amplitude) and randomly active dipoles across the brain surface. In the analysis shown in Figures 5.7 - 5.14, we demonstrated the performance of the constructed beamformer in source reconstruction of one, two and three dipoles configurations, in the cases of spatially close and distant sources and when the neural activity is spatially extended to a single patch and two patches. It has been shown that the temporal dynamics of the sources can also be reconstructed, revealing the original damped oscillatory behavior. The results allow us to conclude that the proposed modification of the beamforming procedure benefits from imposing anatomical constraints and, along with the realistic geometry and conductivity-based forward solution, provides an accurate approach to the inverse problem. In addition, EEG beamforming is compared to MEG beamforming and has been shown in Figure 5.1 to have comparable spatial resolution and one major, though expected, advantage: EEG beamforming is able to detect radial sources. Furthermore, EEG is most sensitive to the radial sources, due to the fact that these sources are located closer to the surface where the electric potential is less distorted by the skull.

The next step was an attempt to overcome the main cause of inaccuracies in beamformers. It is well established that beamformers show poor performance in reconstruction of highly correlated sources, one example of which is in an evoked

auditory task. If an auditory stimulus is fed into both ears, both left and right primary auditory cortices are activated simultaneously, causing the EEG beamformer to erroneously place the widespread source in the center of the brain. For this case we propose to apply the beamformer not to the electric potential but its second spatial derivative, the surface Laplacian, which is known to represent an estimate of the cortical potential. As such, it is much more localized compared to the electric potential distribution on the scalp. This property allows the beamforming algorithm to reduce or completely eliminate the bias connecting the correlated sources and to properly detect source locations as shown in Figure 5.16. The problem of the reconstruction of the time series of the sources is solved by considering a subset of sensors, i.e., the sensors located above one of the hemispheres at a time. As shown in Figure 5.19, when the subsets of sensors are considered separately, the time-courses of the sources can be successfully reconstructed.

Conclusions and Outlook

Different approaches have been taken in the past decades to study the spatiotemporal dynamics of the human brain and determine neural source locations in an attempt to better understand how the human brain functions. In this thesis we carried out a comprehensive simulation study on how beamforming performs when applied to EEG. Several key issues were addressed:

- Since the propagation of the electric potential is greatly affected by the skull conductivity and shape, we constructed a realistic geometry head model from CT and MRI scans of a subject and demonstrated its superior performance by comparison with the spherical models. While spherical models are still being used in clinical applications due to the speed of calculation, realistic geometry models based on boundary and finite element methods are becoming more and more attractive. Beamforming with a boundary element method EEG forward solution, implemented in our work, is computationally intensive only in the preparatory phase, when subject-specific data has to be collected and the beamforming array of forward solutions has to be calculated. When the geometry of the brain and the head tissues are obtained and forward solutions from all possible sources on the brain surface are calculated, the source localization from a given EEG time series at the sensors is fast to compute. The beamforming algorithms were implemented for EEG with spherical, multi-spherical

and realistic geometry models. Comparison shows an increase in accuracy of the source reconstruction when instead of spherical models a more realistic model, based on the boundary element method (BEM), is used. One of the possible directions for future work is to consider the finite element method (FEM) which will allow to take into account the inhomogeneity of the head tissues, especially the skull (e.g. cavities, eye sockets, variations in the conductivity, etc.), which is the main obstacle on the way of the electric potential to the surface of the scalp.

- Anatomical constraints are implemented with the LCMV beamforming algorithm, namely, all source dipoles are assumed to be located on the surface of the white matter with a direction perpendicular to this surface, allowing for a reduction of computation time and placing a proper bias on the EEG source reconstruction. Our simulations show that this method works well for multiple and extended uncorrelated sources and in the presence of noise. It also allows to compare beamforming source localization results for MEG and EEG data derived from the same source distribution. Additional investigations are suggested for extended sources, because when the patch size is increased, it may include opposite walls of sulci in which case field cancelation can be expected.

- Finally, we proposed and theoretically investigated a novel method to detect temporally correlated sources in EEG by using the surface Laplacian in LCMV beamforming. The second spatial derivative of the potential, or surface Laplacian, one of the popular deblurring tools for EEG, is suggested to be used in place of the electric potential in the beamforming algorithm. Our simulations show that it is possible to not only correctly detect the source locations but also to reconstruct the corresponding time series. Preliminary research has shown the possibility of detecting multiple temporally correlated sources and requires further investigation.

Another important step to take in this research is obviously to apply the pro-

posed methodology to real EEG signals and to test the robustness of the method with experimental data obtained in well-controlled tasks. Simple movements or auditory stimulation would be natural first steps, as the locations of sources in these cases are well known from fMRI and MEG source localization and beamforming. Another promising direction could be the simultaneous recording of EEG and MEG, which undoubtedly would increase spatiotemporal resolution of the neural source reconstruction and combine the benefits of both EEG and MEG beamforming.

Bibliography

- [Babiloni et al., 1996] Babiloni, F., Babiloni, C., Carducci, F., Fattorini, L., Onorati, P., Urbano, A. (1996) Spline Laplacian estimate of EEG potentials over a realistic magnetic resonance-constructed scalp surface model. *Electroencephalography and Clinical Neurophysiology*, **98**, 363-373.
- [Baillet et al., 2001] Baillet, S., Mosher, J.C., Leahy, R.M. (2001) Electromagnetic brain mapping. *Signal Processing Magazine, IEEE*, **18-6**, 14-30.
- [de Barros et al., 2006] de Barros, J.A., Carvalhaes, C.G., de Mendonca, J.P.R.F., Suppes, P. (2006) Recognition of words from the EEG Laplacian. *Revista Brasileira de Engenharia Biomedica*, **21**, 143-150.
- [Borgiotti, Kaplan, 1979] Borgiotti, G.V., Kaplan, L.J. (1979) Superresolution of Uncorrelated Interference Sources by Using Adaptive Array Techniques. *IEEE Transactions on Antennas Propagation*, **27**, 842-845.
- [Bradshaw et al., 2001] Bradshaw, L.A., Wikswo Jr., J.P. (2001) Spatial filter approach for evaluation of the surface Laplacian of the electroencephalogram and magnetoencephalogram. *Annals of Biomedical Engineering*, **29**, 202-213.
- [Braitenberg, Schüz, 1991] Braitenberg, V., Schüz, A. (1991) Cortex: Statistics and Geometry of Neural Connectivity, Springer Verlag, Berlin

- [Brookes et al., 2008] Brookes M.J., Mullinger K.J., Stevenson C.M., Morris P.G., Bowtell R. (2008) Simultaneous EEG source localization and artifact rejection during concurrent fMRI by means of spatial filtering. *NeuroImage*, **40**, 1090-1104.
- [Cheyne, Gaetz, 2003] Cheyne, D., Gaetz, W. (2003) Neuromagnetic localization of oscillatory brain activity associated with voluntary finger and toe movements. *NeuroImage*, **19** (Suppl), 1061.
- [Cheyne et al., 2006] Cheyne, D., Bakhtazad, L., Gaetz, W. (2006) Spatiotemporal Mapping of Cortical Activity Accompanying Voluntary Movements Using an Event-Related Beamforming Approach. *Human Brain Mapping*, **27**, 213-229.
- [Dalal et al., 2006] Dalal, S.S., Sekihara, K., Nagarajan, S.S. (2006) Modified beamformers for coherent source region suppression. *IEEE Transactions on Biomedical Engineering*, **53**, 1357-1363.
- [Dale et al., 1999] Dale, A.M., Fischl, B., Sereno, M.I. (1999) Cortical Surface-Based Analysis I: Segmentation and Surface Reconstruction. *NeuroImage*, **9**, 179-194.
- [Delorme, Makeig, 2004] Delorme, A., Makeig, S. (2004) EEGLAB: an open source toolbox for analysis of single-trial EEG dynamics. *Journal of Neuroscience Methods* **134**, 9-21.
- [Ferguson, Stroink, 1997] Ferguson, A.S., Stroink, G. (1997) Factors Affecting the Accuracy of the Boundary Element Method in the Forward Problem. I. Calculating Surface Potentials. *IEEE Transactions on Biomedical Engineering*, **44**, 1139-1155.

- [Fischl et al., 1999] Fischl, B., Sereno, M.I., Dale, A.M. (1999) Cortical Surface-Based Analysis II: Inflation, Flattening and a Surface-Based Coordinate System. *NeuroImage*, **9**, 194-207.
- [Frost, 1972] Frost III, O.L. (1972) An Algorithm for Linearly Adaptive Array Processing. *Proceedings of the IEEE*, **60**, 926-935.
- [Fuchs, 2002] Fuchs, A. (2002) Combining Technologies: The Use of Brain Surfaces. In: *Biomag 2002, Proceedings of the 13th International Conference on Biomagnetism*, H. Nowak, J. Haueisen, F. Geißler, R. Huonker, eds., VDE Verlag, Berlin, pp. 878-880.
- [Fuchs, 2007] Fuchs, A. (2007) Beamforming and its Applications to Brain Connectivity. In: *Handbook of Brain Connectivity*, V.K. Jirsa, A.R. McIntosh, eds., Springer Verlag, Berlin, pp. 357-378.
- [Gevins, 1989] Gevins, A.S. (1989) Dynamic functional topography of cognitive tasks. *Brain Topography*, **2**, 37-56.
- [Gorodnitsky et al., 1992] Gorodnitsky, I.F., Rao, B.D., George, J. (1992) Source Localization in Magnetoencephalography using an Iterative Weighted Minimum Norm Algorithm. *IEEE*, **92**, 167-171.
- [Hämäläinen, Ilmoniemi, 1994] Hämäläinen, M.S., Ilmoniemi, R.J. (1994) Interpreting magnetic fields of the brain: minimum norm estimates. *Medical and Biological Engineering and Computing*, **32**, 35-42.
- [Hämäläinen, Sarvas, 1987] Hämäläinen, M.S., Sarvas, J. (1987) Feasibility of the homogeneous head model in the interpretation of neuromagnetic fields. *Physics in Medicine and Biology*, **32-1**, 91-97.

- [Hämäläinen, Sarvas, 1989] Hämäläinen, M.S., Sarvas, J. (1989) Realistic Conductivity Geometry Model of the Human Head for interpretation of Neuromagnetic Data. *IEEE Transactions on Biomedical Engineering*, **36**, 165-171.
- [Hillebrand, Barnes, 2003] Hillebrand A., Barnes G.R. (2003) The use of anatomical constraints with MEG beamformers. *NeuroImage*, **20**, 2302-2312.
- [Howseman, Bowtell, 1999] Howseman, A.M., Bowtell, R.W. (1999) Functional magnetic resonance imaging: Imaging techniques and contrast mechanisms. *Philosophical Transactions of the Royal Society, London B, Biological Sciences*, **354**, 1179-1194.
- [Huang et al., 2004] Huang, M.X., Shih, J.J., Lee, R.R., Harrington, D.L., Thoma, R.J., Weisend, M.P., Hanion, F., Paulson, K.M., Li, T., Martin, K., Miller, G.A., Canive, J.M. (2004) Commonalities and Differences Among Vectorized Beamformers in Electromagnetic Source Imaging. *Brain Topography*, **16**, 139-158.
- [Koles, 1998] Koles, Z.J. (1998) Trends in EEG source localization. *Electroencephalography and clinical Neurophysiology*, **106**, 127-137.
- [Lin et al., 2006] Lin, F.H., Witzel, T., Ahlfors, S.P., Stufflebeam, S.M., Belliveau, J.W., Hämäläinen, M.S. (2006) Assessing and improving the spatial accuracy in MEG source localization by depth-weighted minimum-norm estimates. *NeuroImage*, **31**, 160-171.
- [Liu et al., 1998] Liu, A.K., Belliveau, J.W., and Dale, A.M. (1998) Spatio-temporal imaging of human brain activity using functional MRI constrained MEG data: Monte Carlo simulations. *Proceedings of the National Academy of Sciences*, **95**, 8945-8950.

- [Mosher, et al., 1992] Mosher, J. C., Lewis, P. S., Leahy, R. M. (1992) Multiple dipole modeling and localization from spatio-temporal MEG data. *IEEE Transactions on Biomedical Engineering*, **39**, 541-557.
- [Mosher et al., 1999] Mosher, J.C., Leahy, R.M., Lewis, P.S. (1999) EEG and MEG: Forward Solutions for Inverse Methods. *IEEE Transactions on Biomedical Engineering*, **46**, 245-259.
- [Nunez, Srinivasan, 2006] Nunez, P., Srinivasan, R. (2006) Electric Fields of the Brain. The Neurophysics of EEG. 2nd ed. Oxford University Press, New York, pp. 317-352.
- [Plonsey, Heppner, 1967] Plonsey, R., Heppner, D.B. (1967) Considerations of quasi-stationarity in electrophysiological systems. *Bulletin of Mathematical Biophysics*, **29**, 657-664.
- [Popescu et al., 2008] Popescu M., Popescu E.A., Chan T., Blunt S.D., Lewine J.D. (2008) SpatioTemporal Reconstruction of Bilateral Auditory Steady-State Responses Using MEG Beamformers. *IEEE Transactions on Biomedical Engineering*, **55**, 1092-1102.
- [Robinson, Vrba, 1999] Robinson, S.E., Vrba, J. (1999) Functional Neuroimaging by Synthetic Aperture Magnetometry (SAM). In: *Recent advances in biomagnetism*, Yoshimoto, T., Kotani, M., Kuriki, S., Karibe, H., Nakasato, N., eds. Tohoku University Press, Sendai, Japan, pp. 302-305.
- [Sarvas, 1987] Sarvas, J. (1987) Basic mathematical and electromagnetic concepts of the biomagnetic inverse problem. *Physics in Medicine and Biology*, **32**, 11-22.

- [Schmidt, 1986] Schmidt, R.O. (1986) Multiple Emitter Location and Signal Parameter Estimation. *IEEE Transactions on Antennas and Propagation*, **34**, 276-280.
- [Sekihara, 1996] Sekihara, K. (1996) Generalized Wiener Estimation of Three-Dimensional Current Distribution from Biomagnetic Measurements. *IEEE Transactions on Biomedical Engineering*, **43**, 281-291.
- [Spencer et al., 1992] Spencer, M.E., Leahy, R.M., Mosher, J.C. and Lewis, P.S. (1992) Adaptive Filters for monitoring localized brain activity from surface potential time series. In: *Proceedings of the 26th Asilomar Conference on Signals, Systems and Computers*, Pacific Grove, CA, pp. 156-161.
- [Toro et al., 2008] Toro, R., Perron, M., Pike, B., Richer, L., Veillette, S., Pausova, Z., Paus, T. (2008) Brain size and folding of the human cerebral cortex. *Cerebral Cortex*, **18(10)**, 2352-2357.
- [Villringer, Chance, 1997] Villringer, A. and Chance, B. (1997) Non-Invasive Optical Spectroscopy and Imaging of Human Brain Function. *Trends in Neuroscience*, **20**, 435-442.
- [van Hoey et al., 1999] van Hoey, G., van de Walle, R., Vanrumste, B., d'Have, M., Lemahieu, I., Boon P. (1999) Beamforming Techniques Applied in EEG Source Analysis. *Proceedings of ProRISC, IEEE*, **10**, 545-549.
- [van Oosterom, Strackee, 1983] van Oosterom, A., Strackee, J. (1983) The Solid Angle of a Plane Triangle. *IEEE Transactions on Biomedical Engineering*, **30**, 125-126.

- [van Veen, Buckley, 1988] van Veen, B., Buckley, K. (1988) Beamforming: A versatile approach to spatial filtering. *IEEE Acoustics, Speech, Signal Processing Magazine*, **5**, 4-24.
- [van Veen et al., 1997] van Veen, B.D., van Drongelen, W., Yuchtman, M., Suzuki, A. (1997) Localization of Brain Electrical Activity via Linearly Constraint Minimum Variance Spatial Filtering. *IEEE Transactions on Biomedical Engineering*, **44**, 867-880.
- [von Helmholtz, 1853] von Helmholtz, H.L.F. (1853) Some laws concerning the distribution of electric currents in volume conductors with applications to experiments on animal electricity. *Proceedings of the IEEE*, transl. by D.B. Geselowitz (2004) **92**, 868-870.
- [Ward et al., 1998] Ward, D.M., Jones, R.D., Bones, P.J., Carroll, G.J. (1998) Enhancement of epileptiform activity in the EEG by 3-D adaptive spatial filtering: Simulations and real data. *Proceedings of 20th Annual International Conference of the IEEE Engineering in Medicine and Biology Society*, **20**, 2116-2119.
- [Wong, Gordon, 2009] Wong, D., Gordon, K. (2009) Beamformer Suppression of Cochlear Implant Artifacts in an Electroencephalography Dataset. *IEEE Transactions on Biomedical Engineering*, **56**, 2851-2857.
- [Zhang, Jewett, 1994] Zhang, Z., Jewett, D.L. (1994) Model Misspecification Detection by Means of Multiple Generator Errors, Using the Observed Potential Map. *Brain Topography*, **7**, 29-39.
- [Zhang, 1995] Zhang, Z. (1995) A fast method to compute surface potentials generated by dipoles within multilayer anisotropic spheres. *Physics in Medicine and Biology*, **40**, 335-349.